Chapter 19 – EXPERIMENTAL INVESTIGATIONS ON THE VFE-2 CONFIGURATION AT DLR, GERMANY

by

Robert Konrath, Christian Klein, Andreas Schröder, Klaus de Groot

19.1 SUMMARY

In the present chapter experimental investigations within the International Vortex Flow Experiment 2 (VFE-2) on a delta wing of 65° sweep angle with sharp as well as with rounded leading edges are described. High resolution surface pressure distributions are measured by means of the Pressure Sensitive Paint (PSP) technique at sub- and transonic speeds (M = 0.4 and 0.8). These tests were complemented by flow field measurements applying Stereo Particle Image Velocimetry (PIV) in different planes above the delta wing. Furthermore, under cryogenic conditions (M < 0.2) the Infrared (IR) and Temperature Sensitive Paint (TSP) techniques are used for the detection of laminar/turbulent transition in the boundary layer. The results were analysed with respect to the onset of the primary vortex on the delta wing with rounded leading edges, the occurrence of an inner vortex, the development of a vortex system consisting of an inner and outer primary vortex, and under transonic conditions to the sudden occurrence of vortex breakdown above the delta wing. Preliminary results of the transition measurements are available which will be discussed, too.

19.2 INTRODUCTION

The objectives of the International Vortex Flow Experiment 2 (VFE-2) are to provide experimental flow data by using modern measurement techniques for comparison with results from state-of-the-art CFD calculations, see Chapter 17. At the beginning of the 1980's the first VFE [19-3][19-5] was carried out on a cropped 65° delta wing-fuselage combination. Since in the last fifteen years considerable progress has been achieved in the numerical calculation of vortical flows [19-7][19-8][19-22] a new International Vortex Flow Experiment (VFE-2) has been proposed by Hummel and Redeker [19-9]. Since 2003 the VFE-2 is being carried out within the framework of the task group AVT-113 of NATO's Research and Technology Organization. Using NASA's definition of a 65° delta wing geometry [19-2] the investigations within VFE-2 now also consider delta wings with rounded leading edges (Figure 19-1). In the present investigations the sharp as well as the medium radius leading edge ($r/\bar{c}$ = 0.0015) is considered.

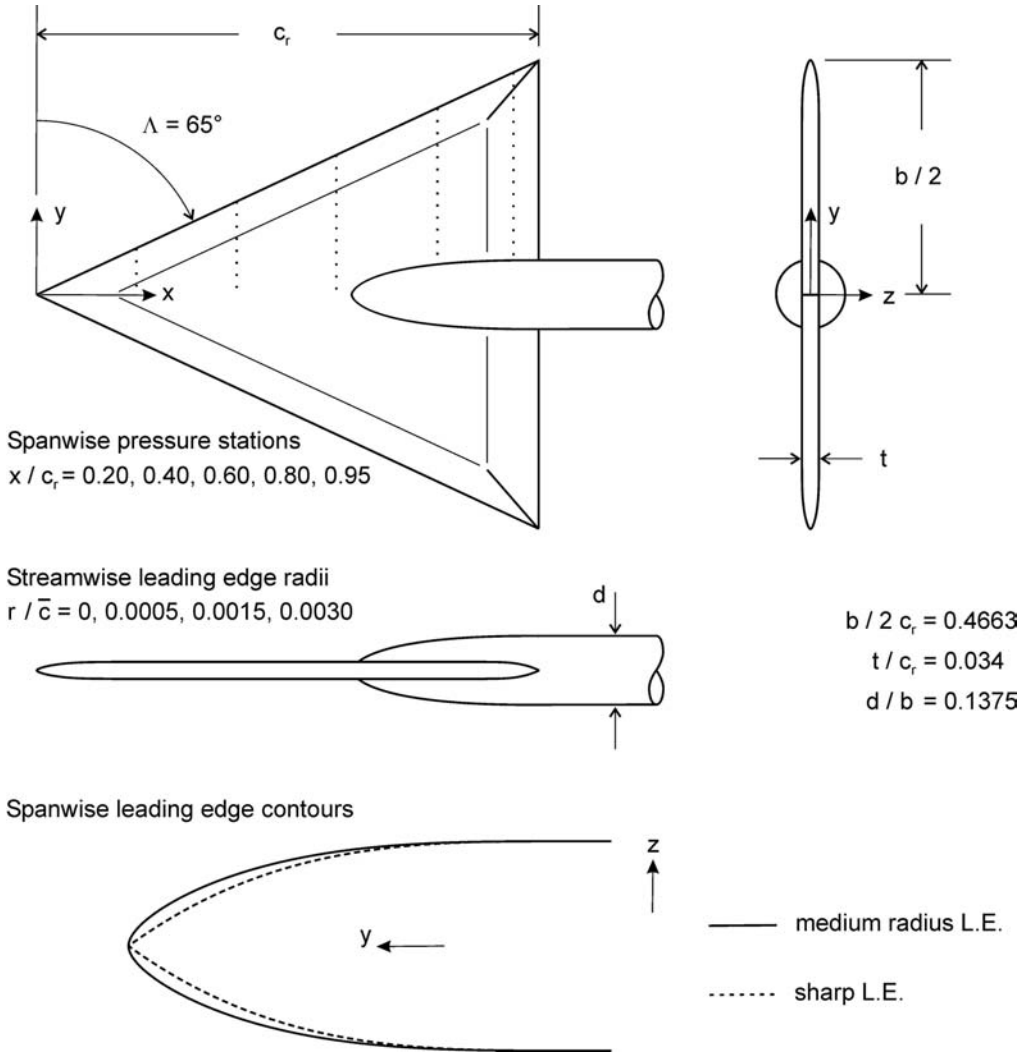

Figure 19-1: Geometry of VFE-2 Configuration (Details of contours are described in [19-2]).

The developments achieved so far at optical flow measurement techniques such as the Particle-Image Velocimetry (PIV), the Pressure Sensitive Paint (PSP), the Infrared (IR) or the Temperature Sensitive Paint under cryogenic conditions (TSP) techniques allow to cope with many technical problems arising especially in industrial wind tunnels. These techniques are able to capture a huge amount of experimental data during a wind tunnel test campaign. With PSP the pressure distribution on a whole surface can be determined giving much more insight in details of the flow topology than would be possible by discrete pressure taps. PIV provides instantaneous as well as time averaged flow velocity fields in different planes of the flow and enables the detection of large and small spatial flow structures. The Infrared and Temperature Sensitive Paint techniques provide high resolution information of transition for large areas on wings. The parallel application of these methods can help to save wind tunnel costs in order to get the necessary data for flow analysis or comparison with CFD results [19-15].

In the present study three measurement campaigns were performed by DLR in two different wind tunnels. The investigations started with PSP measurements in the transonic wind tunnel at Göttingen (DNW-TWG) of

the German-Dutch Wind tunnel association (DNW), which serve as "pathfinder" tests. For the tests in the TWG NASA provided its ¾ scale 65° delta wing model of c_r = 0.49 m (Model No. 1, see overview in Chapter 17 and Figure 19-1). The PSP results give first information of the flow topology over the delta-wing for a large range of angles of attack at sub- and transonic speeds. In a second test campaign Stereo-PIV measurements were performed. The used angles of attack and locations of the measurement planes for PIV were selected on the basis of the PSP results. The measured velocity fields provide details of the flow field. A last measurement campaign took place in the cryogenic wind tunnel in Cologne (DNW-KKK) using a delta wing model built by the Technical University of Munich (TUM) of c_r = 0.98 m (Model No. 2). The original objective of these tests was to investigate the effects of high Reynolds numbers at M < 0.2 on the flow. However, first CFD calculations show that the knowledge of transition on the delta wing is strongly needed in order to improve the numerical prediction of the flow. So, it was decided to apply IR and TSP in the KKK, too, although the construction of the TUM model was not particularly suitable for such tests. For all measurements the models were coated by different paints, which has to be taken into account when comparing the results with other data.

In the following Section 19.3 the test conditions and the results of the measurements in the transonic wind tunnel in Göttingen (DNW-TWG) are described. First the differences of flow separation at the leading edge for sharp and rounded edged delta wing are discussed. The onset of the primary vortex and chord positions of its origin is determined on the basis of the PSP results in dependency of angle of attack, Mach and Reynolds number. For the rounded leading edge at subsonic Mach numbers a flat inner vortical structure occurs close to the surface above the delta wing which is described using PSP and PIV. From this vortical structure an inner vortex develops after the onset of the primary vortex. The resulting vortex system is described in detail considering the effects of angle of attack and Reynolds number. The Q-criterion is applied to the PIV data to visualize vortices and to calculate the vortex circulation. At transonic speed (M = 0.8) results showing a sudden change of the pressure and velocity distributions at high angles of attack, which probably are related to the occurrence of vortex breakdown caused by an interaction between shock waves and the primary vortex, are discussed too. Further results form the TWG tests can be found in [19-16] and [19-17]. In Section 19.4 the measurements and preliminary results of the cryogenic wind tunnel in Cologne (DNW-KKK) are described. The transition on the delta wing is discussed, particularly, for the rounded leading edge case.

19.3 INVESTIGATIONS IN THE TRANSONIC WIND TUNNEL IN GÖTTINGEN

19.3.1 Test Conditions and Measurement Setups

19.3.1.1 Wind Tunnel Facility and Model Instrumentation

Two measurements campaigns were carried out in the Transonic Wind tunnel in Göttingen (DNW-TWG) which is a continuously running closed-circuit wind tunnel. The test section of 1 m x 1 m size is enclosed by a plenum chamber, within which the total pressure can be set in a range from 30 000 to 150 000 Pa, so that Reynolds and Mach number effects can be studied independently. Different test sections are available enabling sub-, trans- and supersonic flow conditions. The perforated test section is used here, because small observation windows can be installed in the upper and lower wall behind which the PSP cameras and light sources are positioned. The walls of the perforated test section incorporate 60 degree inclined holes of 10 mm diameter, giving a porosity of 5.6%. However, no suction was applied during the tests. For the perforated test section, the turbulence level was measured being between 1 and 1.4% depending on Mach number. The top and bottom wall of the test section are inclined, i.e. ±0.25° and ±0.563° for M = 0.4 and M = 0.8 respectively, such that the cross section size increases downstream in order to compensate the increasing boundary layer at

the walls. The lateral walls were equipped with 50 mm thick Schlieren windows of 450 mm x 950 mm in size getting optical access for PIV.

For the tests in the transonic wind tunnel (DNW-TWG) the ¾ scale model (c_r = 0.4902 m, b = 0.4572 m, $\bar{c}$ = 0.3268 m) was provided by NASA. It incorporates interchangeable leading edge segments. The sharp as well as one rounded leading edge with the medium radius ($r/\bar{c}$ = 0.0015) were used for the current investigations. The model is equipped with 183 pressure taps, mainly arranged at constant chord stations of x/c_r = 0.2, 0.4, 0.6, 0.8 and 0.95. Three PSI modules with each having 64 ports measure the static pressures at the tap locations. The quoted accuracy of the PSI modules is about ±50 Pa, e.g. 0.05% of the instrument maximum pressure. A 15°-bent sting was used to extend the positive angle of attack range. The model sting was equipped with strain gages configured for two moment bridges to measure the normal force and pitching moment in order to estimate the bending of the sting. The resulting effective angle of attack of the model could be determined with an accuracy of ±0.02°.

19.3.1.2 Application of Pressure Sensitive Paint

The first test campaign took place in 2004 and comprises surface pressure, which serve as “pathfinder” tests. By applying a pressure sensitive paint to a wind tunnel model surface pressure distributions can be determined by measuring the luminescence intensity of the molecule emission. Two different paints are applied for the current tests. Both are based on a two-color formulation with pyrene as the pressure sensitive luminophore and with Europium as reference dye. For the tests with rounded leading edges the DLR02 paint is used, which consists of a screen layer and an active layer giving a total thickness of about 60 µm. A further developed paint was applied for the tests with the sharp edged delta-wing model, which consists of a single layer only with a reduced paint thickness of 40 µm. Small windows in the top and bottom wall of the test section are used on the current PSP-setup (see [19-18] or [19-14] for details) for cameras and illumination (Figure 19-2). Only a small region close to the leading edge was not accessible optically because of the large angle between the viewing direction of the cameras and the surface normal. Therefore, the C_p data at spanwise locations larger than 99.2 % of the span width is blanked out in the results.

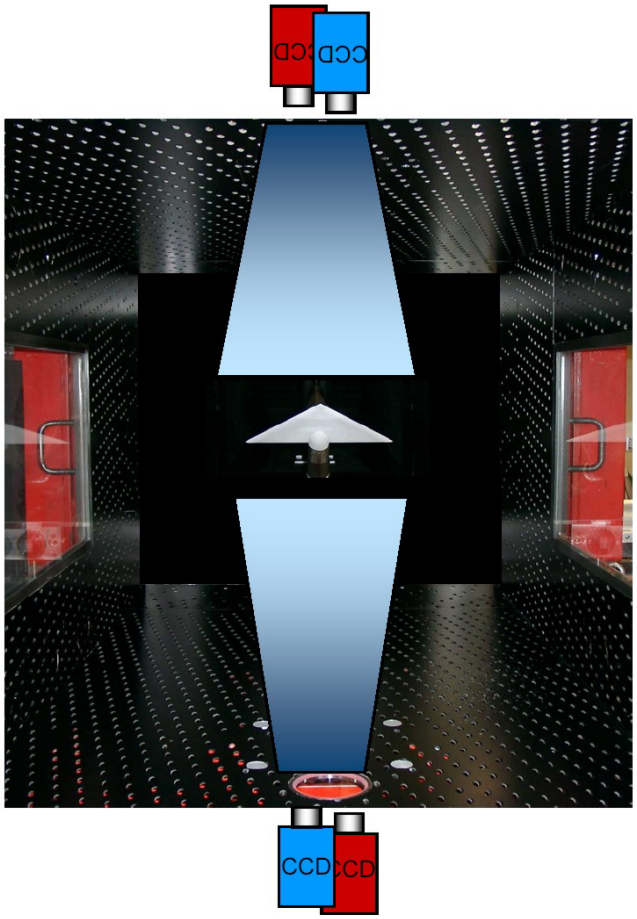

Figure 19-2: Coated Delta-Wing Model in the Test Section of the DNW-TWG and Arrangement of PSP Cameras.

The comparison between the results of PSP and the PSI system of the wind tunnel at the pressure tap locations show a good agreement. The standard deviation is better than 1000 Pa. This includes a temperature dependency of the paint of 300 – 500 Pa/K [19-13]. Because of the higher temperature drop below the strong primary vortices, this leads to slightly underestimated suction peak heights in the PSP distributions as compared to the PSI results. For the PSP measurements the sharp as well as the medium radius leading edge, two Mach and two Reynolds numbers are used for a large range of angles of attack (Table 19-1).

Table 19-1: Test Cases for PSP Measurements in the TWG

Leading Edge	Sharp / Medium Radius
M	0.4 / 0.8
R_{mac}	2×10^6 / 3×10^6
α (nominal)	10° – 25° in steps of 1°

19.3.1.3 Application of Particle Image Velocimetry

In a second test campaign, which took place in 2005, Stereo-PIV was applied to the flow above the delta wing model. The velocity fields in different planes perpendicular to the model axis are determined. For the PIV tests the delta wing model was coated, too, with a specific black paint to avoid light flare on the surface coming from the impinging laser light sheet that allows PIV measurements down to the surface. The thickness of the paint is ca. 90 µm, which is slightly higher than that of the PSP paint. The PIV set-up is shown in Figure 19-3. The light-sheet and the cameras can be translated along the model axis during wind tunnel operation. The arrangement also incorporates rotary plates in order to adjust quickly the set-up for different angles of attack, see [19-18] or [19-26] for details.

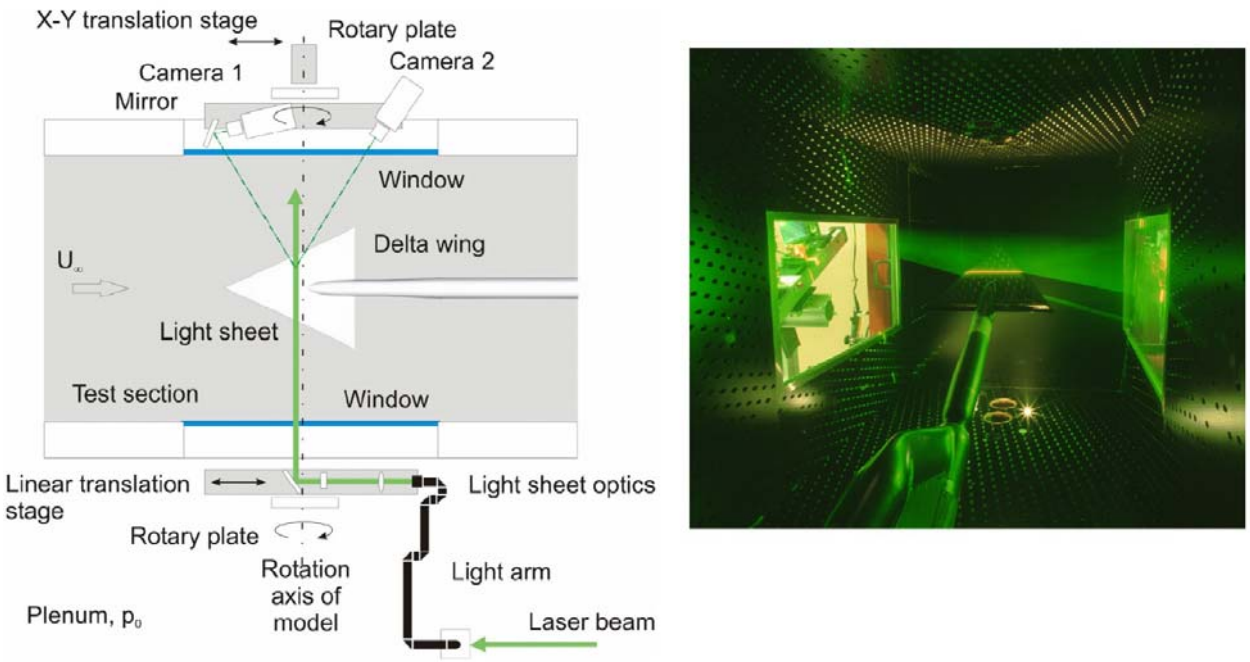

Figure 19-3: Stereoscopic PIV Arrangement at the TWG and Picture from Inside the Perforated Test Section Showing the Coated Delta-Wing, Light Sheet and the Two Lateral Schlieren Windows.

The uncertainty of the velocities after the stereoscopic reconstruction can be estimated for the current arrangement to be less than 3% for the *u* and *w* component and less than 2% for the *v* component with respect to the maximum velocity in the flow field. These values also include a maximum error of about 1% due to uncertainties in the determination of the camera positions. The spatial resolutions of the measurements are listed in the table below in dependency of field-of-view. The same test cases as chosen for PSP were taken with respect to leading edge shape, Mach and Reynolds number. Four different angles of attack and different chord locations were selected (Table 19-2).

Table 19-2: Test Cases for PIV Measurements in the TWG

Leading Edge	**Sharp / Medium Radius**
M	0.4 / 0.8
R_{mac}	$2 \cdot x\ 10^6$ / 3×10^6
α (nominal)	10°, 13°, 20°, 25°
Cross plane locations	x/c_r = 0.35 – 0.9 in steps of 0.05 / 0.1
Field-of-view (*y,z*)	146 mm x 60 mm for α = 10°, 13°, 20° 219 mm x 108 mm for α = 25°
Spatial resolution (*y,z*)	3.6 mm x 2 mm for α = 10°, 13°, 20° 5.3 mm x 3.6 mm for α = 25°

19.3.1.4 Vortex Identification for Flow Field Analysis

In order to extract coherent vortical structures within complex flow fields different identification schemes can be used by evaluating the velocity gradient tensor $\nabla\vec{u}$ such as the λ_2-criterion. In the current case the Q-criterion is applied to the PIV data, whereas Q denotes the positive second invariant of $\nabla\vec{u}$ [19-1]:

$$Q = \frac{1}{2}\left[(\nabla\cdot\vec{u})^2 - tr\left(\nabla\vec{u}^{\,2}\right)\right]. \tag{19-1}$$

For an incompressible flow Q is defined as:

$$Q = \frac{1}{2}\left[\|\Omega\|^2 - \|S\|^2\right], \tag{19-2}$$

whereas S and Ω are the tensors of rate of strain and vorticity respectively and correspond to the symmetric and anti-symmetric components of the velocity tensor:

$$\nabla\vec{u} = S + \Omega = \frac{1}{2}\left(\nabla\vec{u} + \nabla\vec{u}'\right) + \frac{1}{2}\left(\nabla\vec{u} - \nabla\vec{u}'\right). \tag{19-3}$$

Hence, Q constitutes a local indicator for the dominance of the rotation rate (Q > 0) compared to the strain rate. Since only planar velocity data is available the third derivatives are assumed to be negligible and the equation of Q reduces to:

$$Q = u_{1,1}u_{2,2} - u_{1,2}u_{2,1}. \tag{19-4}$$

The Q-criterion is used to define an area to calculate the circulation of a single vortex using the surface integral over the vorticity $\vec{\omega}$:

$$\Gamma = \int_{-\infty}^{\infty} \vec{\omega} \cdot \vec{n} \, dA \,. \tag{19-5}$$

To estimate the circulation of a single vortex the integration area is restricted using the criterion $Q > 0.1\ Q_{max}$, whereas Q_{max} is the particular maximum Q-value close to the vortex center. In the current case the chosen threshold of 10% excludes the shear layer forming the primary vortex. This is demonstrated in Figure 19-4, which shows a slice of the velocity field through a primary vortex with the distributions of the out-of-plane vorticity ω_x and the Q-values. The black lines indicate the boundary of the integration area for calculating the circulation corresponding to the 10% drop of the Q-value within the vortex.

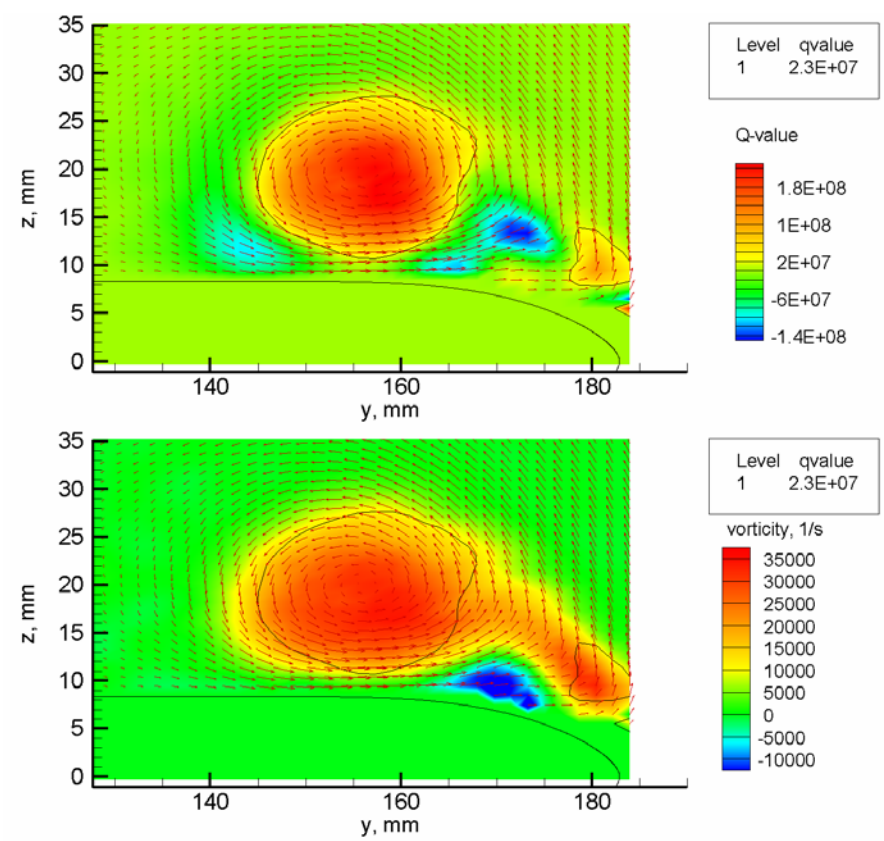

Figure 19-4: Velocity Vector Field of Primary Vortex for the Delta Wing with Medium Radius Leading Edges at $x/c_r = 0.8$ for M = 0.4, R_{mac} = 2 Million, α = 13.3° (top) Q-value and (bottom) Out-of-Plane Vorticity Distribution. The black line indicates the boundary of the integration area used for calculating the vortex circulation.

19.3.2 Results

19.3.2.1 Comparison of PSI Results Obtained in TWG by DLR and NTF by NASA

In the following the PSI data obtained at TWG is compared to the wind tunnel results of NASA obtained at the NTF [19-2] for the case: delta wing with medium leading edge, M = 0.85, R_{mac} = 6 million. In the NTF the large

version of the delta-wing model of c_r = 0.6536 m was used. Figure 19-5 shows the PSI results for angles of attack of 13.4°, 20.6° and 24.8°. The last angle differs to the NTF result by 0.2°. In the results of the TWG the Mach numbers varies by about ±1% and the Reynolds number is at maximum 4% smaller than the set values.

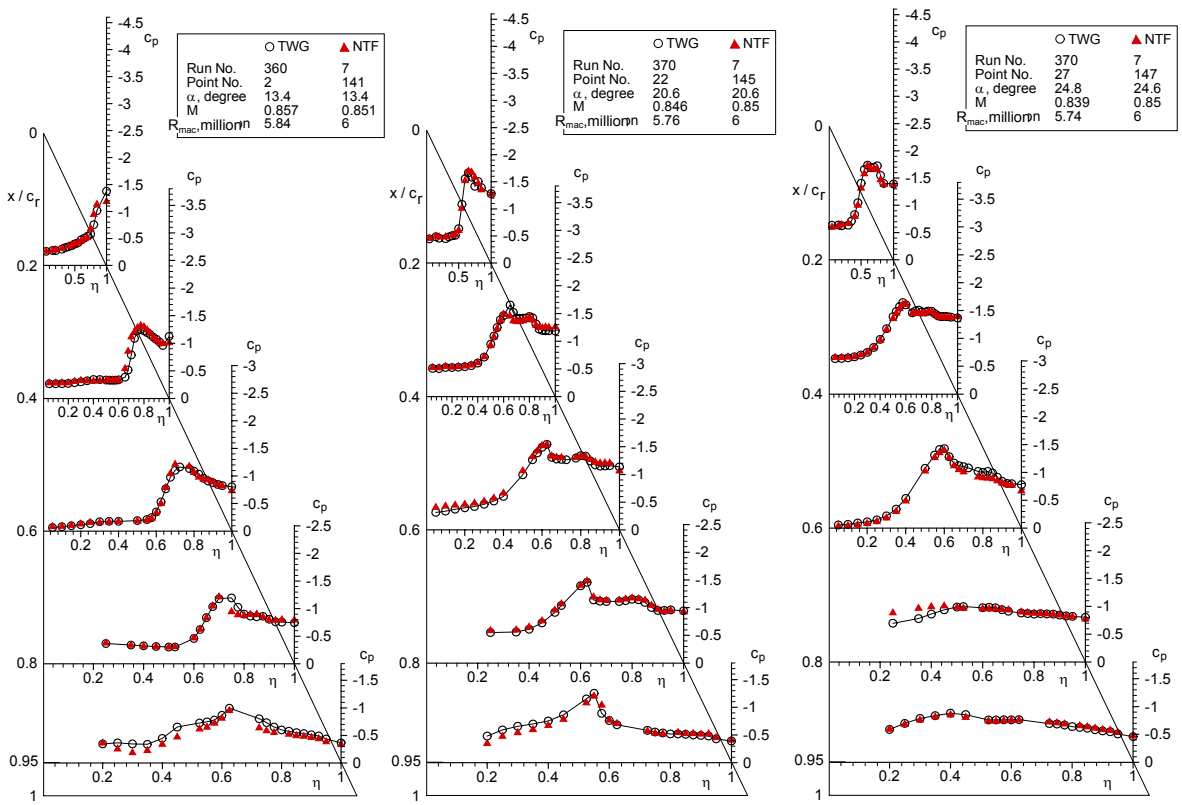

Figure 19-5: Comparison of PSI Pressure Distributions Obtained in TWG and in NTF (NASA) [19-2] of the Uncoated Delta Wing with Rounded Leading Edges at M = 0.85 and R_{mac} = 6 Million for Three Different Angles of Attack.

For all angles of attacks the results agree very well. Differences exists only in the foremost section of α = 13.4°, where the onset of the leading edge separation seems to start a little earlier in the NTF and at α = 20.6° in the section x/c_r = 0.4, where the peak value of the primary vortex is slightly higher in the TWG. At α = 24.8° a breakdown of the primary vortex occurs downstream of x/c_r = 0.6, which is represented in both wind tunnels.

19.3.2.2 Effects of Model Coating

The approximate thickness of the DLR 02 PSP paint is 60 µm ± 5µm. That is about 12 percent of the radius of the rounded leading edge and should be taken into account at analysis of the data and comparison with numerical results. Differences in the pressure distributions can be found only in the case of the rounded leading edge for the small Mach number of 0.4 and at medium angles of attack. Figure 19-6 shows a comparison of PSI results obtained with the un-coated and the coated model with medium radius leading edges. At low angle of attack of α = 10.1° the results of the coated and the un-coated model agree very well. In both cases an attached flow exits

at the leading edge. At higher incidence of $\alpha = 13.2°$ larger deviations in the pressure plots can be seen. For this particular case, where an inner and outer suction peak occur (further described in Section 19.3.2.3), the flow is very sensitive to small changes of the model shape. The leading edge separation starts earlier in case of the un-coated model, which can be explained by the smaller leading edge radius. The pressure distributions differ at most after the onset of the leading edge separation, i.e. $x/c_r > 0.2$. At higher angles of attack the pressure distribution matches again as shown in Figure 19-6 for $\alpha = 20.5°$.

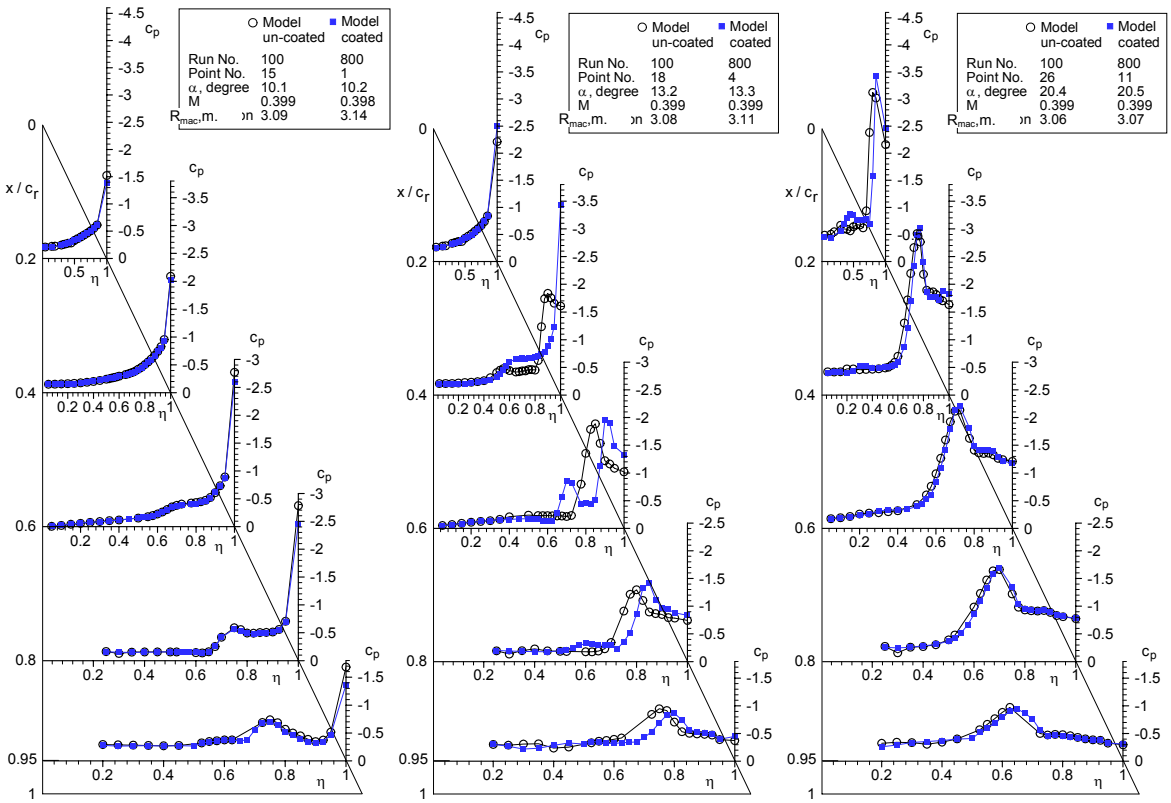

Figure 19-6: Comparison of PSI Pressure Distributions of the Un-Coated and the Coated Delta Wing with Rounded Leading Edges at M = 0.4 and R_{mac} = 3 Million for Three Different Angles of Attack.

19.3.2.3 Onset of Primary Vortex

For delta wings with sharp leading edges the flow separates at the leading edges already at small angles of attack. The shear layer rolls up and the flow re-attaches to the model surface. The primary vortices are formed starting at the apex of the delta wing. Depending on the angle of attack the attachment line is located at the center line of the delta wing or at a spanwise location between the primary vortex and the delta wing center line. Underneath the primary vortices an outboard directed flow establishes. After having passed the suction peak, the steep adverse pressure gradient towards the leading edge causes another flow separation and counter-rotating secondary vortices are formed.

In the case of rounded leading edges the flow separation is no longer fixed to the leading edges. The onset of the primary vortex becomes dependent on the leading edge radius, the angle of attack, the Reynolds and the

Mach number [19-20][19-21], see also Chapter 18. With increasing angle of attack the flow at the leading edge first separates at the rear part of the wing, where the ratio of the leading edge radius over the local wing span is small (VFE-2 configuration with constant leading edge radius). The onset of the primary vortex occurs at a specific incidence when the flow separates effectively. Its origin moves upstream with increasing angle of attack until it reaches the wing apex. In Figure 19-7 the PSP result for a delta wing with sharp as well as with medium radius leading edges are plotted. The suction peaks of the primary vortices are clearly visible, which starts for the sharp edged delta wing at the wing apex and in the rounded leading edge case at $x/c_r = 0.6$.

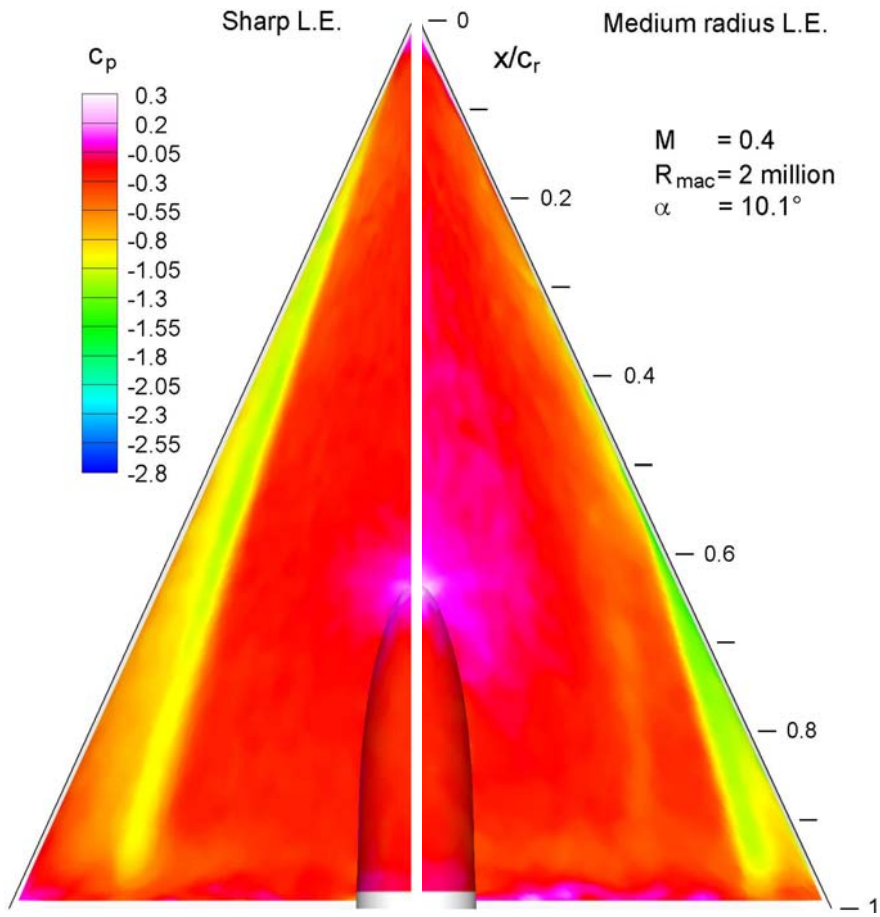

Figure 19-7: Comparison of Surface Pressure Distributions Obtained with PSP at Suction Side of Delta Wing with Sharp (left) and Medium Radius (right) Leading Edge (M = 0.4, R_{mac} = 2 million, α = 10.1°).

Using the PSP results, the chord locations of the primary vortex origins are determined at the starboard side of the wing. The results are plotted in Figure 19-8 against α in dependency of the Mach and Reynolds number. For M = 0.4 and R_{mac} = 3 million the onset of the primary vortex first takes place between α = 11.2° and 12.3°.

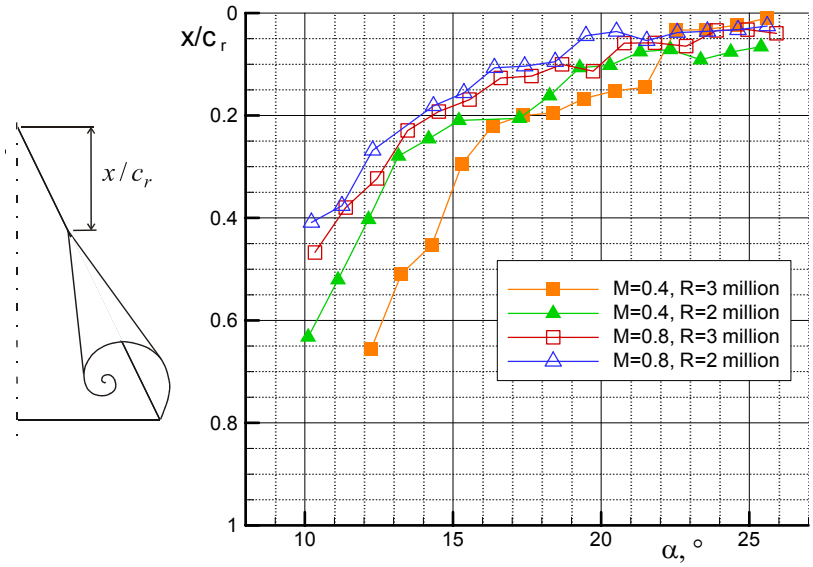

Figure 19-8: Origin Positions of Primary Vortex for α > 10° Obtained from PSP Results for the Delta Wing with Medium Radius Leading Edge for M = 0.4 and 0.8 and R_{mac} = 2 and 3 Million.

Its origin is located at about $x/c_r = 0.65$ for $\alpha = 12.3°$. After its onset, the vortex origin moves quickly towards the wing apex with increasing angle of attack until a chord position of about $x/c_r = 0.3$ is reached; i.e. $\alpha = 15.3°$. Passing this chord position the vortex origin moves more gradually upstream and asymptotically approaches a location close to the wing apex. The plot of M = 0.4 and R_{mac} = 2 million in Figure 19-4 has a similar slope, however, shifted to lower angles of attack by about 2°. This shows that the onset of the primary vortex is postponed for higher Reynolds numbers. The plots for the transonic cases show that the Mach number has an opposite effect on the vortex onset. Also, the differences between both curves of R_{mac} = 2 and 3 million are marginal for M = 0.8 in comparison to the subsonic case. The gradients of the curves, particularly for M = 0.4, show that the location of the primary vortex is very sensitive to small changes of angle-of-attack for chord positions smaller than $x/c_r = 0.3$.

19.3.2.4 Occurrence of Inner Vortical Structure

For the VFE-2 delta wing with rounded leading edges another vortex develops in the subsonic case inboard of the leading edge. Figure 19-9 shows the PSP results for M = 0.4, R_{mac} = 3 million and $\alpha = 10.2°$. In this case the onset of the primary vortex takes place first at an angle of attack between 11.2° and 12.2°. However, in the pressure distribution of Figure 19-8 a suction peak can be clearly seen, which is located inboard of the leading edge. In difference to the footprint of a primary vortex (s. Figure 19-6) this suction peak forms a line parallel to the leading edge with increasing peak height towards the trailing edge.

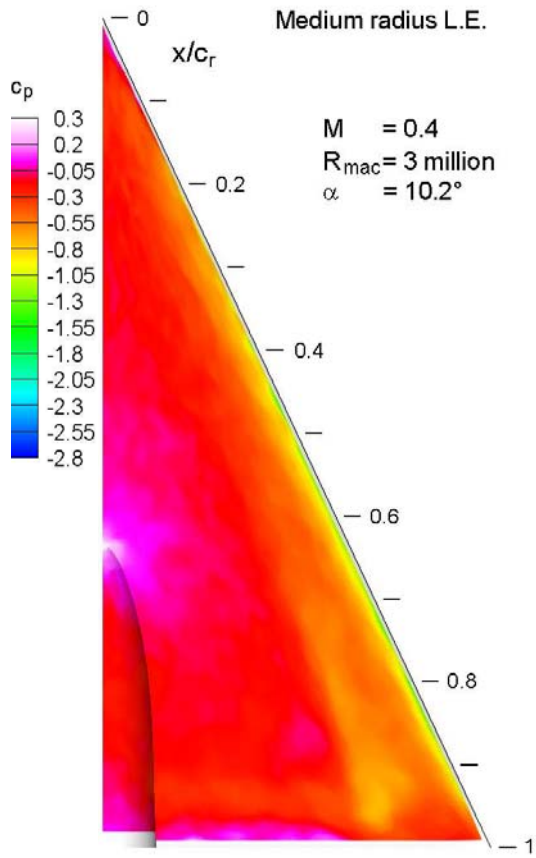

Figure 19-9: Surface Pressure Distribution Obtained with PSP at the Suction Side of Delta Wing with Medium Radius Leading Edge for M = 0.4, R_{mac} = 3 Million and α = 10.2°.

In Figure 19-10 the PIV results are plotted from x/c_r = 0.5 to 0.9 together with the PSP result. It shows an inner vertical structure which increases downstream in size and circulation strength; see later blue dashed line in Figure 19-15. Details of the velocity field at a chord station of x/c_r = 0.6 are shown in Figure 19-11. Close to the model surface the time averaged flow field shows a flat vortical structure spreading in the spanwise direction with increasing vorticity towards the leading edge. The corresponding Q-value distribution reveals that this structure consists of several discrete vortices as indicated in Figure 19-11. Particularly, the outboard located vortices in this plot are fed with vorticity from the outer flow. Mainly these vortices produce the suction peak in the pressure distribution and increase in size and circulation strength further downstream.

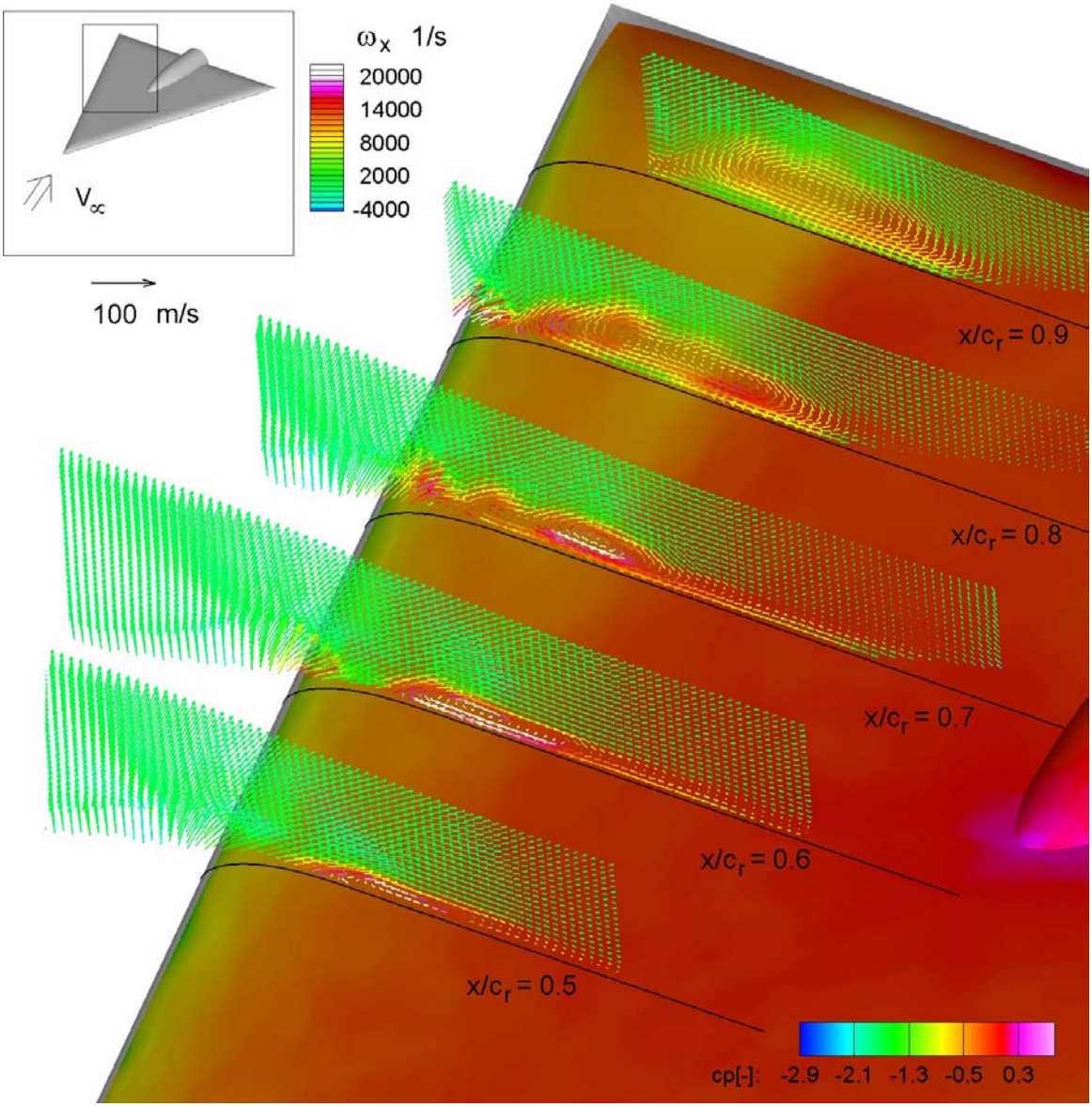

Figure 19-10: Time Averaged Pressure, Velocity and Vorticity Distributions above the Delta Wing with Rounded Leading Edges for α = 10.2°, M = 0.4 and R_{mac} = 3 Million. The in-plane velocity vectors are plotted in different planes perpendicular to the delta wing axis. The color of the vectors corresponds to the out-of-plane vorticity. The colors at the surface are related to the local pressure coefficient.

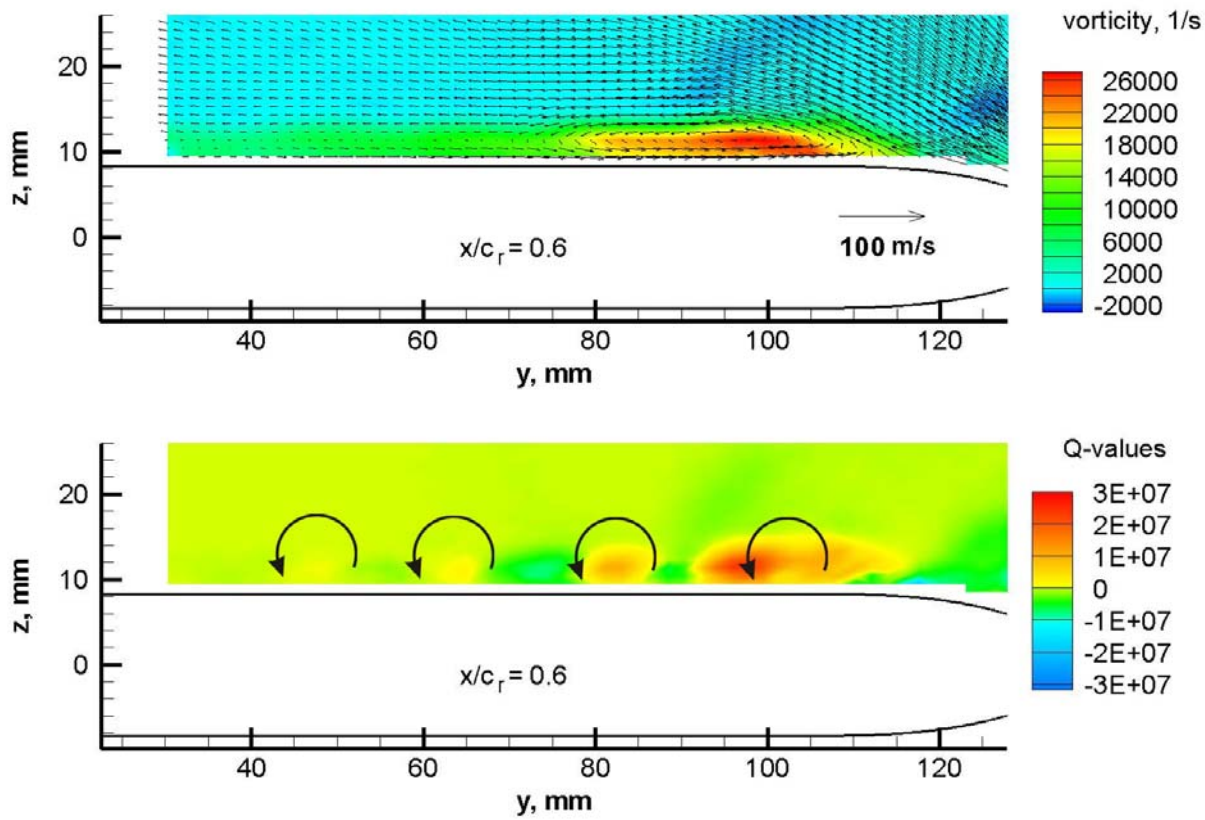

Figure 19-11: Time Averaged PIV Result at x/c_r = 0.6 above the Delta Wing with Medium Radius Leading Edges and M = 0.4, R_{mac} = 3 Million and α = 10.2° (top) Velocity and Vorticity Distributions (bottom) Q-value Distribution.

This inner vortical structure was not detectable for the delta wing with sharp leading edges that could be explained by the existence of the primary vortex starting at the apex just at small angles of attack which might inhibit the development of an inner vortical structure. However, inner vortices are also not detectable for the transonic cases (M = 0.8) regardless of the leading edge radius.

19.3.2.5 Formation of an Inner and Outer Primary Vortex

The flow topology above the delta wing with medium radius leading edges for M = 0.4 and R_{mac} = 3 million as discussed in the previous section changes at higher angles of attack, when the onset of the outer primary vortex takes place, see also Chapter 35. This is case at an angle of attack of α = 13.3° where the origin of the primary vortex is located at about x/c_r = 0.5 (Figure 19-12). Now, the footprint of the inner vortical structure in the pressure distributions has changed. Its maximum pressure peak height is reached just downstream of the origin of the outer primary vortex and drops down further downstream.

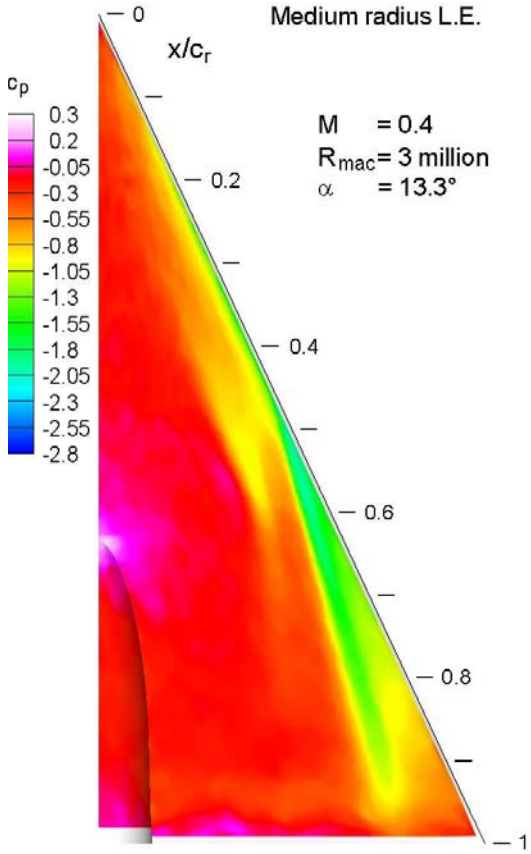

Figure 19-12: Surface Pressure Distribution Obtained with PSP at the Suction Side of Delta Wing with Medium Radius Leading Edge for M = 0.4, R_{mac} = 3 Million and α = 13.3°.

In Figure 19-13 the time averaged velocity and vorticity distributions are plotted of the delta wing in different planes. In the foremost shown chord station of $x/c_r = 0.4$, i.e. upstream the origin of the primary vortex, the inner vortical structure can be seen again as a flat vortex close to the surface similar to the case at $\alpha = 10.2°$ as described in the former section. At the leading edge an attached flow exists, whereas a local flow separation being embedded within the boundary layer may exist, which is not resolved by the used PIV and PSP setup.

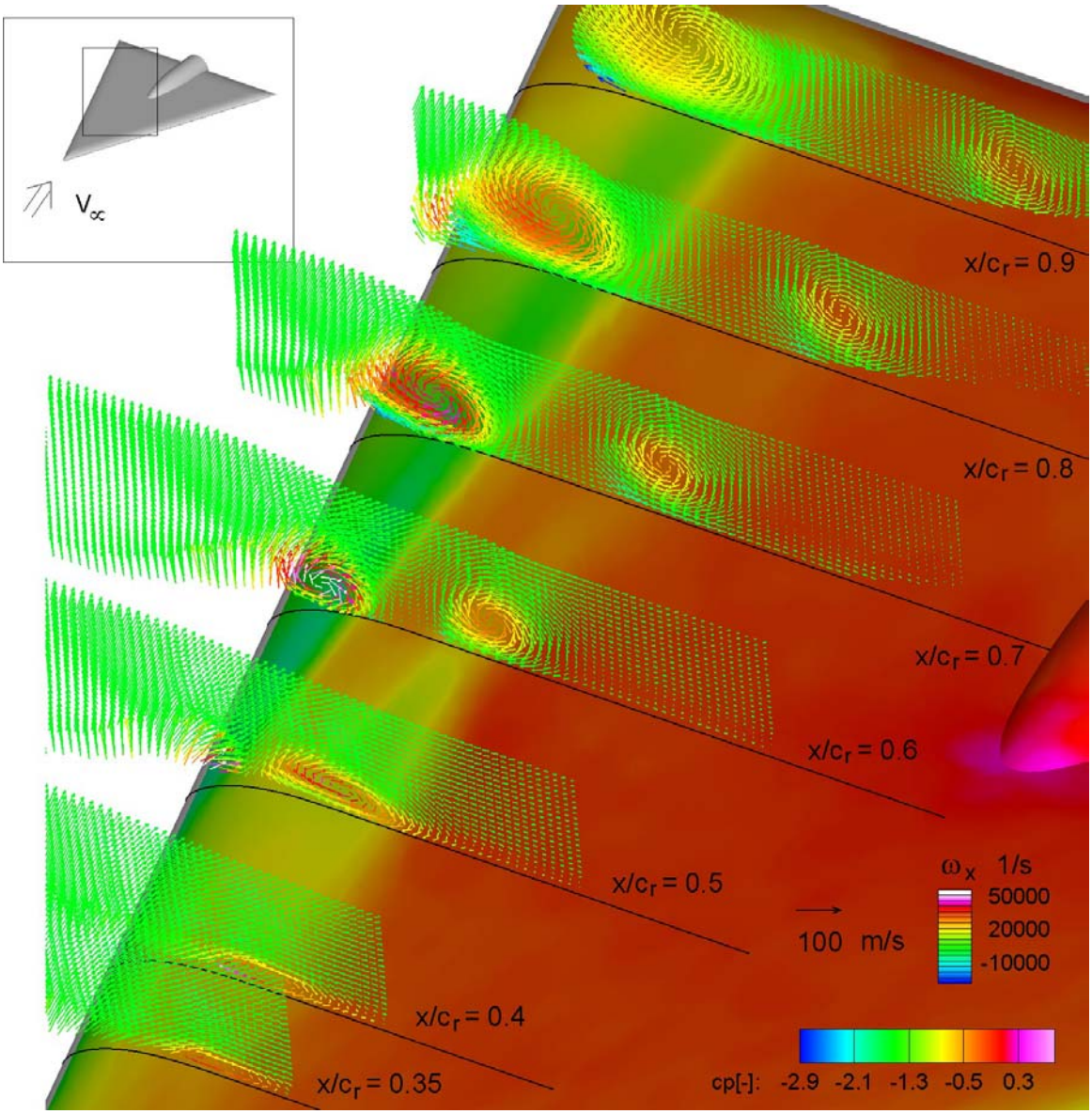

Figure 19-13: Time Averaged Pressure, Velocity and Vorticity Distributions above the Delta Wing with Rounded Leading Edges for α = 13.3°, M = 0.4 and R_{mac} = 3 Million. The in-plane velocity vectors are plotted in different planes perpendicular to the delta wing axis. The color of the vectors corresponds to the out-of-plane vorticity. The colors at the surface are related to the local pressure coefficient.

The velocity field at the chord station of $x/c_r = 0.5$ shows the primary vortex at an early state close the leading edge. Between the outer primary vortex and the inner vortical structure the flow reattaches to the surface and again separates. The inboard directed flow in the vicinity of the inner vortical structure now has changed with respect to the flow direction and velocity magnitude, so that the outer vortices of the inner vortical structure detach from the surface.

Therewith, the co-rotating vortices forming the inner flat vortical structure partly are able to merge and an inner circular vortex is formed, which can be seen in the velocity field at $x/c_r = 0.6$. Now, two co-rotating vortices of approximately the same size can be observed; i.e. an inner and outer vortex. Between both vortices a re-attachment and separation line exists at the surface. Further downstream the inner and outer vortices remain separated and do not merge (s. Figure 19-14, $x/c_r = 0.6$ to 0.8). With increasing size of the primary vortex a focus point is formed between the inner and outer vortex in the velocity field, so that at the surface an outboard directed flow establishes.

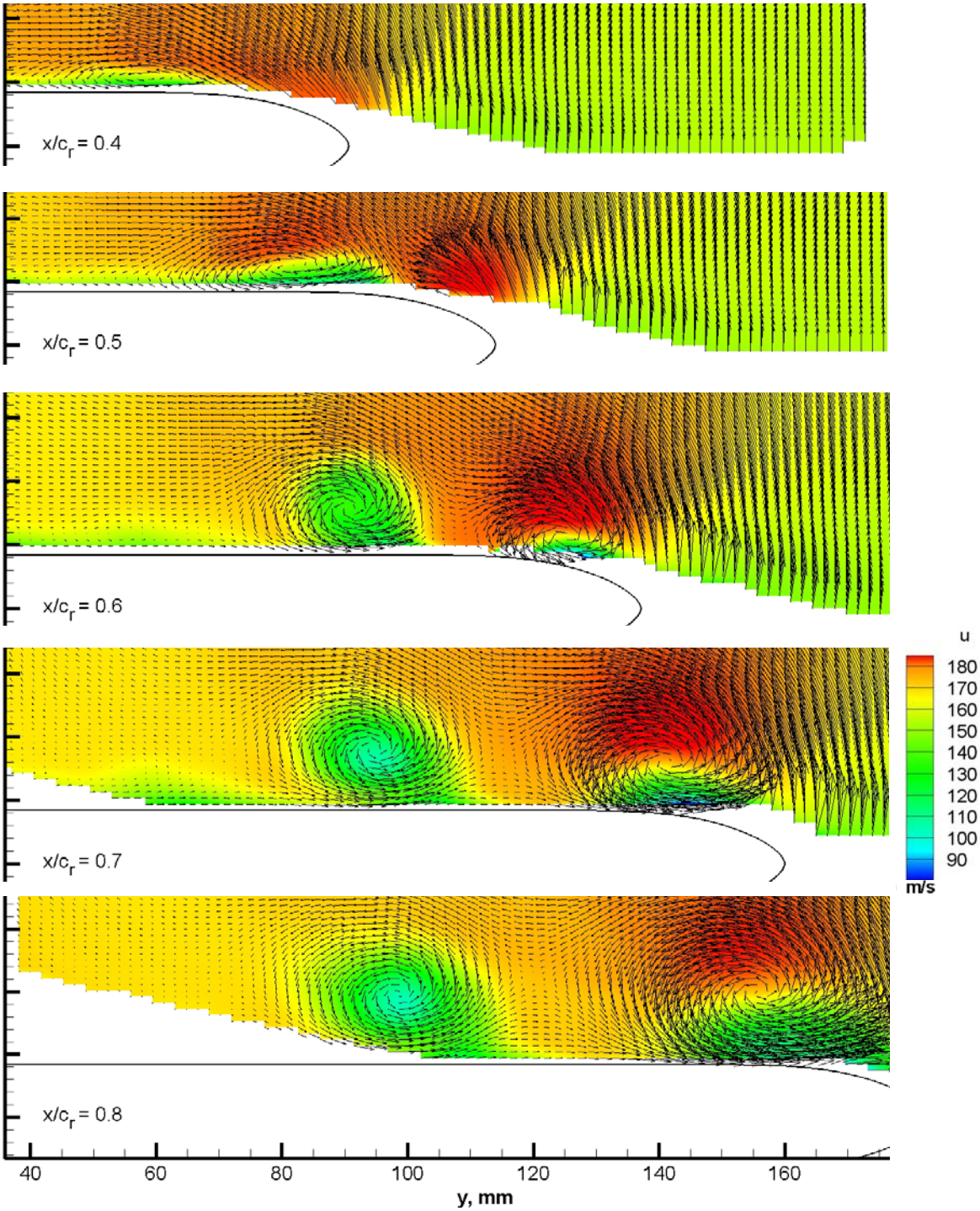

Figure 19-14: Time Averaged Velocity Fields at Different Chord Positions above the Delta Wing with Medium Radius Leading Edges for M = 0.4, R_{mac} = 3 Million and α = 13.3°. The color is related to the out-of-plane velocity u.

In Figure 19-15 the calculated circulations of the inner and outer vortices are plotted against the chord position for different Reynolds numbers and angles of attack. The dashed magenta line corresponds to the inner vortex for the current case. It shows that the circulation of the inner vertical structure first increases in a downstream direction until the primary vortex (solid magenta line) occurs. However, not all of the circulation contained in the inner vortical structure goes into the newly formed inner vortex, as the step in the dashed magenta line between $x/c_r = 0.5$ and 0.6 indicates. In the velocity field at $x/c_r = 0.7$ (Figure 19-14), obviously parts of the inner vortical structure can be detected inboard of the inner vortex.

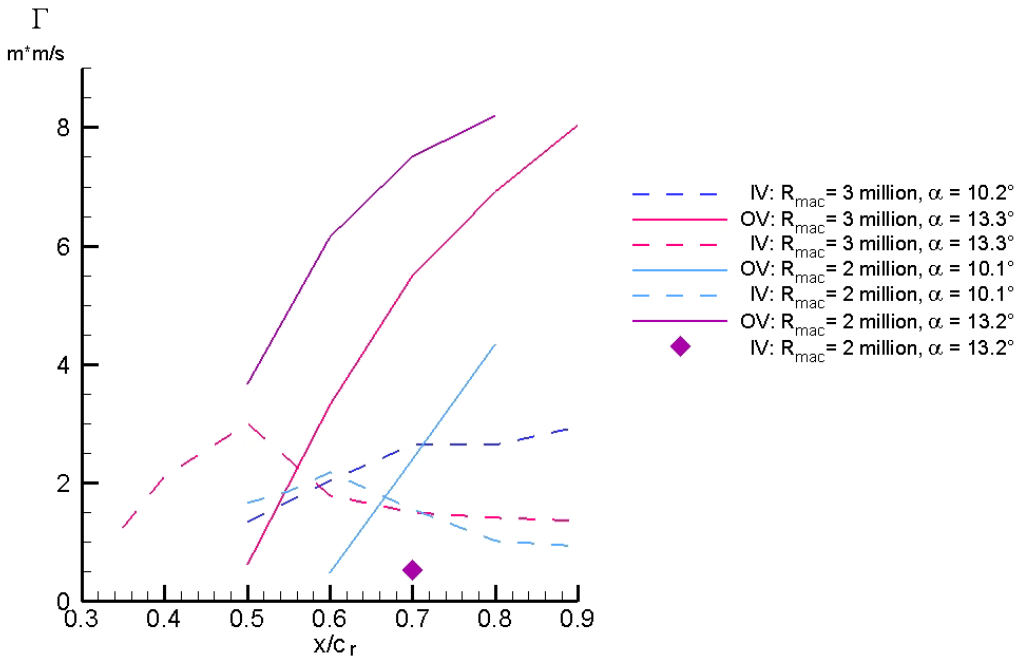

Figure 19-15: Calculated Circulations of the Inner Vortical Structure or the Inner Vortex (IV, dotted lines) and the Outer Primary Vortex (OV, solid lines) against Chord Position for the Medium Radius L.E. and M = 0.4.

Whereas the circulation of the primary vortex continuously increases in a downstream direction (solid magenta line in Figure 19-15), the circulation of the inner vortex decreases slightly. Therefore, after the flow separates effectively at the leading edge vorticity is fed mainly into the primary vortex and not into the inner vortex.

19.3.2.6 Effects of Angle-of-Attack on Vortex System Above Delta Wing with Rounded Leading Edges

In Figure 19-16 the surface pressure distributions are shown for M = 0.4, R_{mac} = 3 million and angles of attack from 10.2° to 25.6°. The first PSP result for $\alpha = 11.2°$ shows an attached flow at the leading edge. In comparison with the result for $\alpha = 10.2°$ in Figure 19-8 the inboard suction peak is stronger, which indicates that the strength of the inner vertical structure increases with increasing angle of attack as long as the onset of a primary vortex has not taken place.

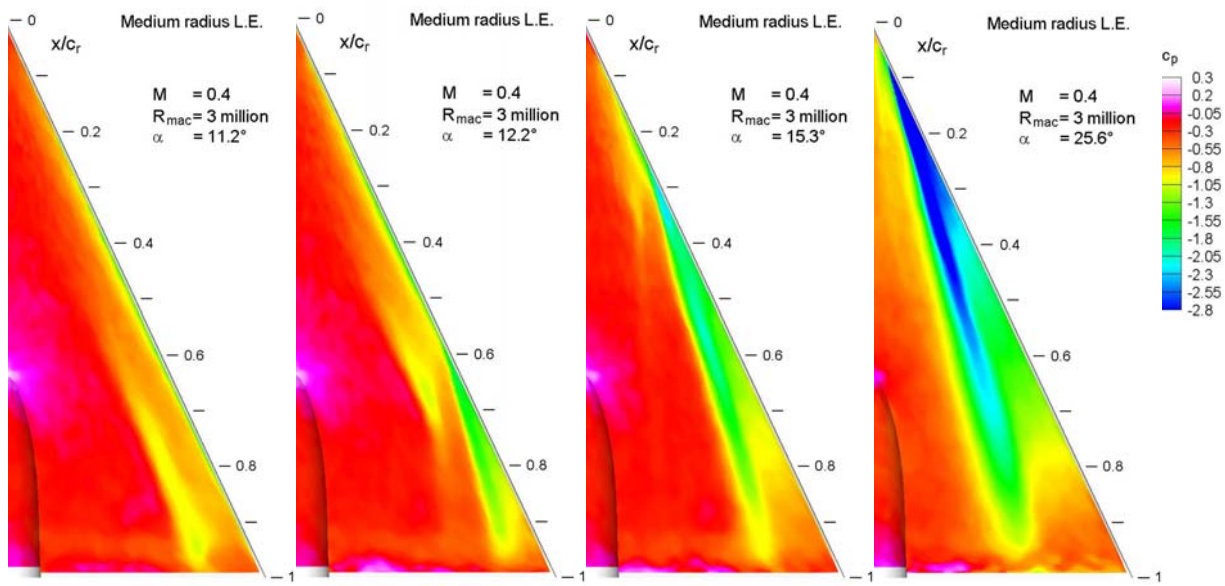

Figure 19-16: Surface Pressure Distributions Obtained with PSP at the Suction Side of the Delta Wing with Medium Radius Leading Edges for Different Angles of Attack (M = 0.4, R_{mac} = 3 million).

The onset of the primary vortex occurs at α = 12.2°. With increasing angle of attack the origin of the primary vortex moves upstream, whereas the footprint of the inner peak is shifted upstream accordingly. Although the inner suction peak height increases with increasing angle of attack for a specific chord position upstream the onset of the primary vortex as stated above, the maximum peak height produced by the inner vortex weakens (s. Figure 19-16, α = 12.2° to 25.6°). This effect can be explained by the quick upstream movement of the primary vortex, since vorticity is no longer fed into the inner vortical structure downstream the primary vortex origin. This can be quantified by comparing the resulting circulation values of the inner vortex in Figure 19-15 for R_{mac} = 2 million, i.e. Γ = 0.5 m^2/s for α = 13.2° (origin of the primary vortex: x/c_r = 0.25) and Γ = 1 m^2/s for α = 10.2° (origin of the primary vortex: x/c_r = 0.6).

19.3.2.7 Effects of Reynolds Number on Vortex System Above Delta Wing with Rounded Leading Edges

Figure 19-17 shows a corresponding series of pressure distributions as shown in Figure 19-16 (R_{mac} = 3 million), however, for a lower Reynolds number of R_{mac} = 2 million. Lowering the Reynolds number promotes the flow separation at the leading edge. Therefore, the onset of the primary vortex starts earlier and the origin of the outer primary vortex is shifted upstream by reducing the Reynolds number. As discussed formerly in Section 19.3.2.3 a more upstream located origin of the primary vortex leads to a lower circulation strength of the inner vortex, since after the occurrence of the primary vortex vorticity is fed mainly into the outer primary vortex and no longer into the inner vortical structure. This results in much lower peak values in the pressure distributions of the inner vortex in the low Reynolds number case. From Figure 19-14 it follows that the circulation is Γ = 1.4 m^2/s for R_{mac} = 3 million and α = 13.3° (origin of the primary vortex: x/c_r = 0.5), which is about three times higher than that for the case of R_{mac} = 2 million and α = 13.2°. Figure 19-18 shows the flow topology above the delta wing for the lower Reynolds number and α = 13.2°. Since the origin of the primary vortex is located more upstream the inner vortex is located more inboard in comparison to the corresponding case for R_{mac} = 3 million (Figure 19-13).

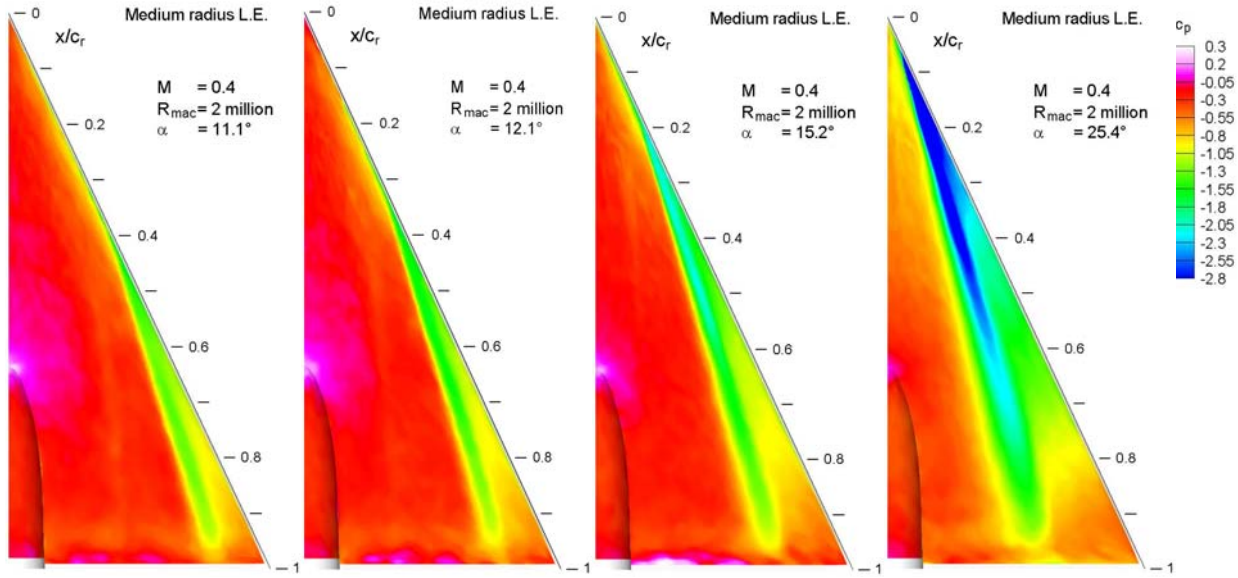

Figure 19-17: Surface Pressure Distributions Obtained with PSP at the Suction Side of the Delta Wing with Medium Radius Leading Edges for Different Angles of Attack (M = 0.4, R_{mac} = 2 million).

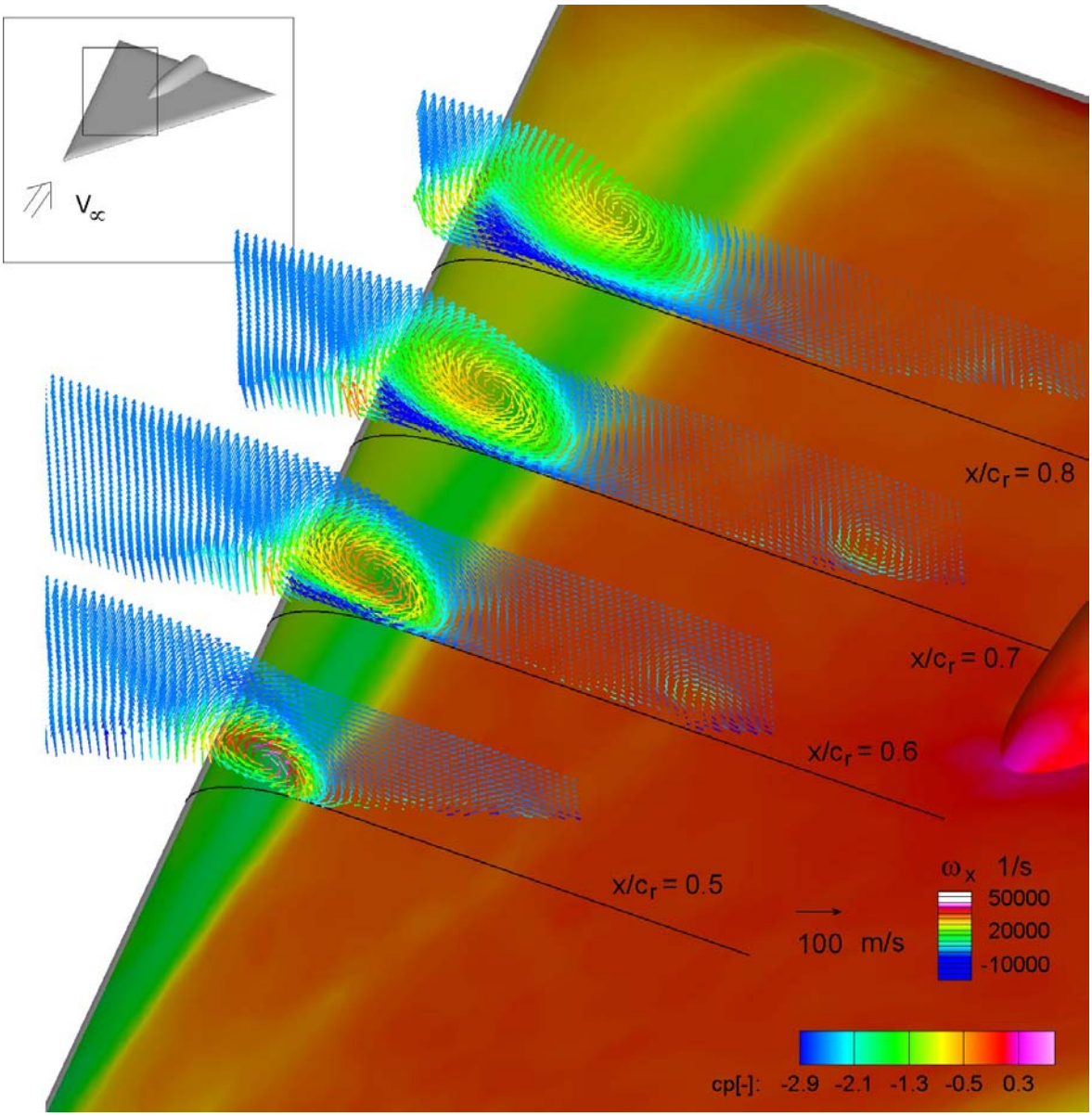

Figure 19-18: Time Averaged Pressure, Velocity and Vorticity Distributions above the Delta Wing with Rounded Leading Edges for α = 13.3°, M = 0.4 and R_{mac} = 2 Million. The in-plane velocity vectors are plotted in different planes perpendicular to the delta wing axis. The color of the vectors corresponds to the out-of-plane vorticity. The colors at the surface are related to the local pressure coefficient.

The circulation strength of the inner vortex formed downstream the origin of the primary vortex is mainly affected by the onset and streamwise position of the primary vortex. However, it is also important for which combination of angle of attack and Reynolds number a specific position of the primary vortex results. The amount of circulation fed into the inner vortical structure, i.e. upstream the primary vortex, depends also on the angles of attack, such that with increasing angle of attack the loss of circulation in the resulting inner vortex, i.e. downstream the primary vortex origin, caused by the according upstream movement of the primary

vortex is partly compensated. This is obviously not the case when the same upstream shift of the primary vortex is achieved by reducing the Reynolds number. The circulation plots in Figure 19-15 for the inner vortical structure of R_{mac} = 2 and 3 million and similar angles of attack, i.e. α = 10.1° and 10.2° respectively, are nearly identical which shows the strength of the inner vortical structure to be less sensitive to the Reynolds number upstream the primary vortex, i.e. $x/c_r \leq 0.6$. This explains the much weaker pressure peaks produced by the inner vortex for R_{mac} = 2 million in comparison to the cases of R_{mac} = 3 million.

19.3.2.8 Vortex Breakdown Above the Delta Wing in Transonic Flow

At the transonic speed of M = 0.8 the flow is much more complex, because the flow above the delta wing reaches supersonic speeds and shock waves occur [19-6], [19-25], see also Chapter 29. Figure 19-19 shows the pressure distributions for the sharp edged delta wing for different angles of attack. At α = 24.1° the footprints of the primary and secondary vortex originating from the wing apex are clearly visible. Plotted, are also constant lines of the sonic pressure coefficient c_p^*. This shows that the outboard directed flow underneath the primary vortex close to the surface is supersonic, so that probably in front of the secondary vortex a cross-flow shock wave is located.

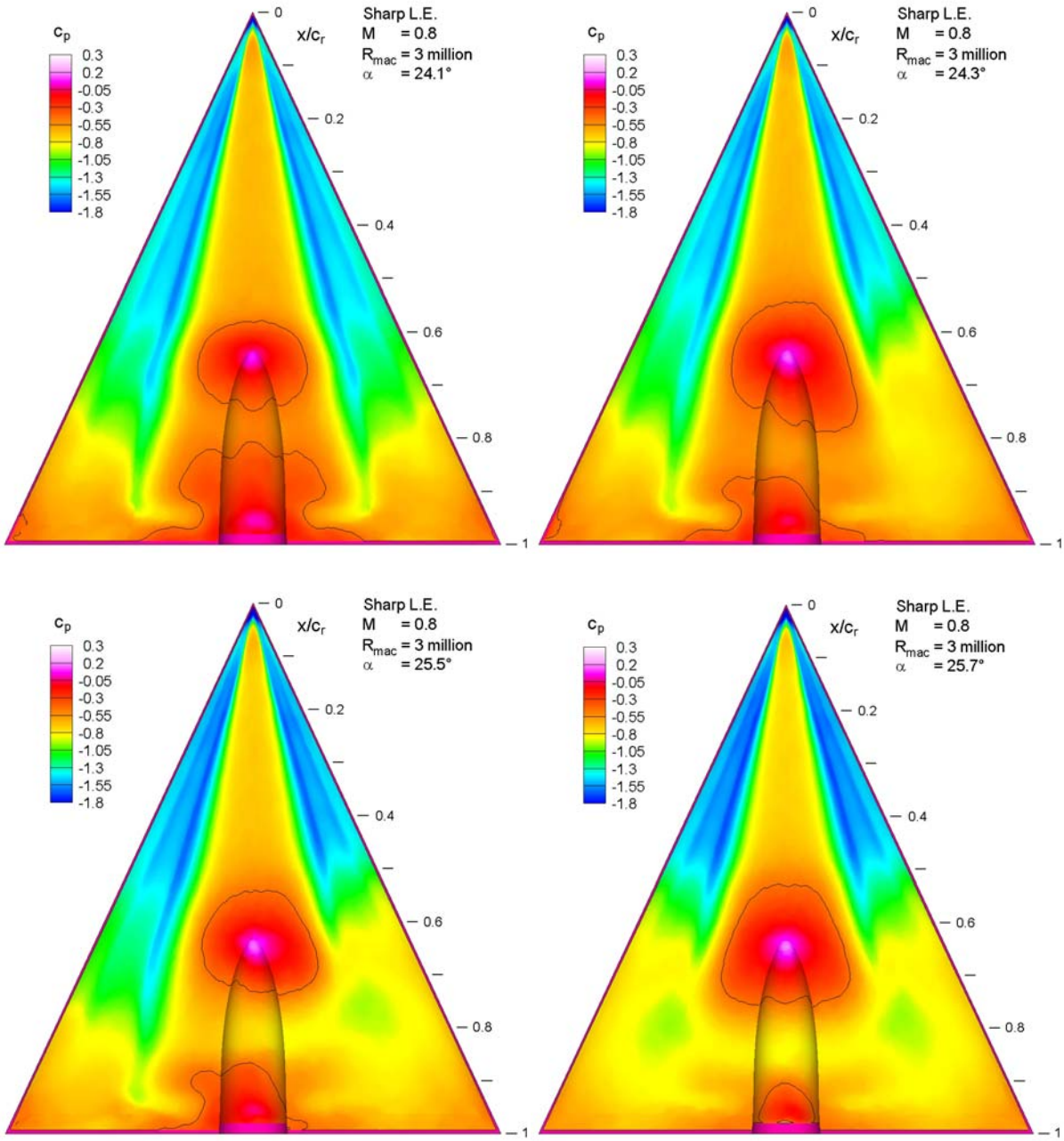

Figure 19-19: Surface Pressure Distributions Obtained with PSP at the Suction Side of the Delta Wing with Sharp Leading Edges in 0.2° Steps of Angles of Attack (M = 0.8, R_{mac} = 3 Million). The black contour lines indicate the sonic pressure coefficient C_p* = -0.43.

In Figure 19-20 the velocity and vorticity distributions are plotted at x/c_r = 0.6 for an angle of attack of α = 25.7° showing the counter-rotating secondary vortex underneath the primary vortex. Also plotted are negative values of the divergence of the in-plane velocity vectors ($\nabla \cdot \vec{v}$) which gives an indication of the location and shape of a cross-flow shock wave.

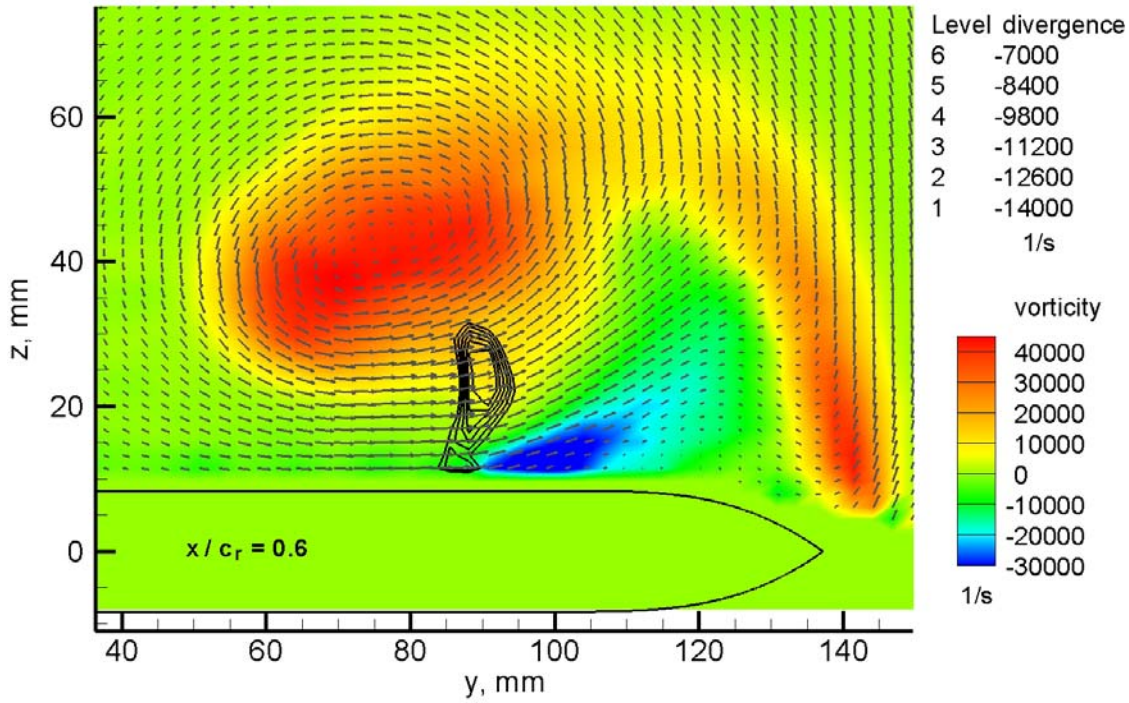

Figure 19-20: Time Averaged Velocity and Vorticity Distributions for the Delta Wing with Sharp Leading Edges at $x/c_r = 0.6$ ($M = 0.8$, $R_{mac} = 3$ Million, $\alpha = 25.7°$). The color of the vectors corresponds to the out-of-plane vorticity. The block contour lines are related to the divergence of the in-plane velocity vectors.

The contour lines of the sonic pressure coefficient in the center of the delta wing give an indication of a terminating shock wave in front of the sting fairing, i.e. about $x/c_r = 0.55$, and a second one closer to the trailing edge downstream of $x/c_r = 0.8$. Increasing the angle of attack by only 0.2° the pressure distribution changes rapidly and becomes unsymmetric (s. Figure 19-19, $\alpha = 24.3°$). Following the suction peak of the primary vortex at the starboard side the peak enlarges suddenly downstream at a chord position of about $x/c_r = 0.7$ and the pressure increases. This gives reason to presume the occurrence of a vortex breakdown [19-27], which may the result from an interaction between the primary vortex and the terminating shock wave in front of the sting. This presumption is also proven by the fact that such an abrupt change of the pressure distribution does not occur in the subsonic cases as shown for example in Figure 19-16 for the delta wing with rounded leading edges and an angle of attack of $\alpha = 25.6°$. Please, notice also that this pressure change takes place by increasing the angle of attack by only $\alpha = 0.2°$. However, the assumed vortex breakdown first occurs only at the starboard side of the wing, which shows that this flow situation seems to be very sensitive to small misalignments of the model or minor imperfections of the model geometry. The pressure distributions become again symmetric at an angle of attack of $\alpha = 25.7°$. Again this takes place after an increase of angle of attack of only 0.2° (Figure 19-19). In Figure 19-21 the corresponding velocity distributions for $\alpha = 25.7°$ are plotted against the pressure distribution.The velocity field upstream the presumed vortex breakdown is shown for $x/c_r = 0.55$. The outward directed flow underneath the primary vortex separates at about $y = 135$ mm ($\eta = 0.85$) and a secondary vortex is formed. The flow field downstream the vortex breakdown at $x/c_r = 0.75$ shows a large region of reverse flow (up to $u = -60$ m/s), which is typically the case in the region of vortex breakdown.

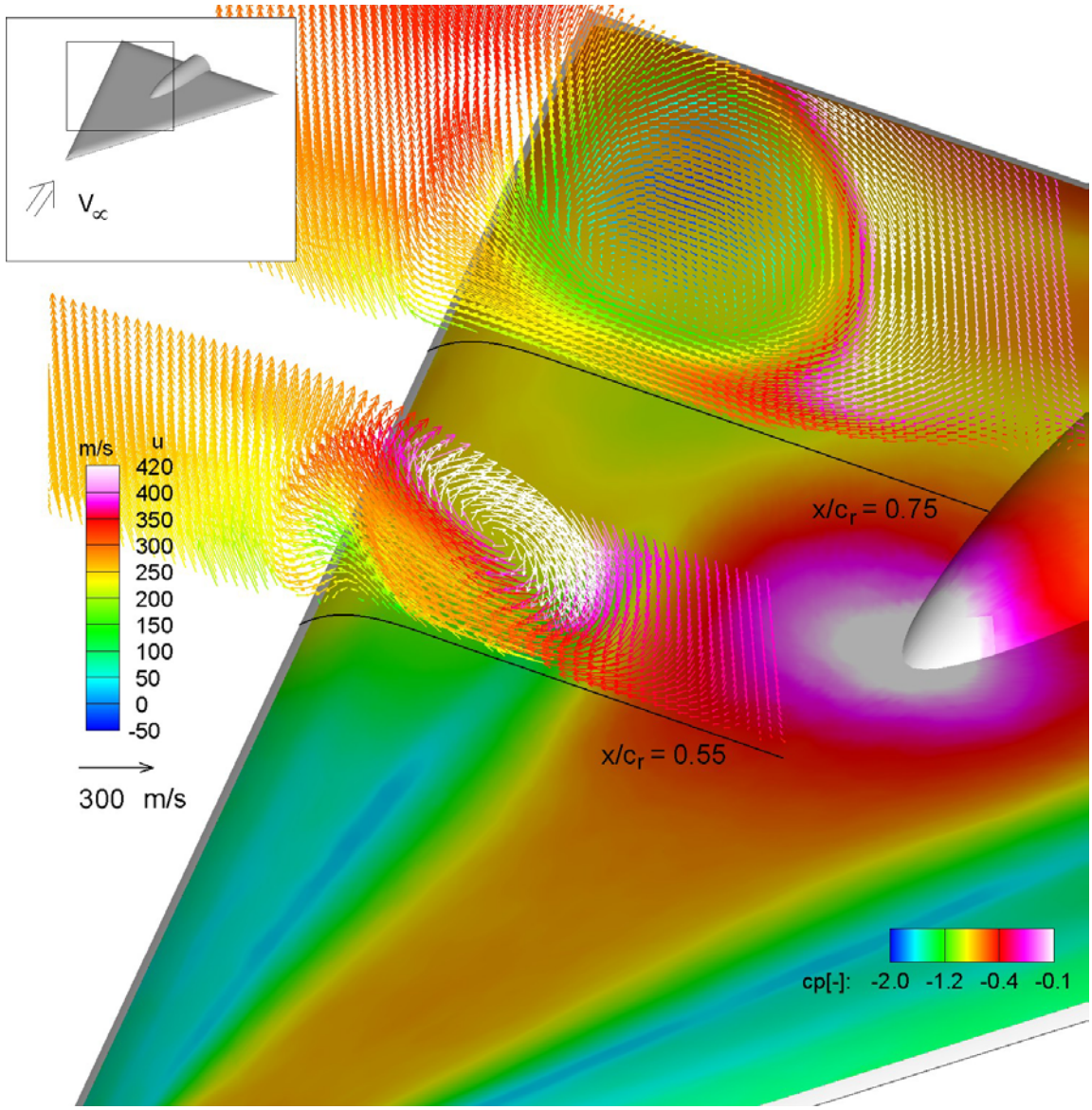

Figure 19-21: Time Averaged Pressure and Velocity Distributions above the Delta Wing with Sharp Leading Edges for M = 0.8, R_{mac} = 3 Million and α = 25.7°. The in-plane velocity vectors are plotted in different planes perpendicular to the delta wing axis. The color of the vectors corresponds to the out-of-plane velocity. The colors at the surface are related to the local pressure.

19.4 INVESTIGATIONS IN THE CRYOGENIC WIND TUNNEL IN COLOGNE

19.4.1 Test Conditions and Measurement Setups

19.4.1.1 Wind Tunnel Facility and Model Instrumentation

The last measurement campaign was carried out in the Cryogenic Wind tunnel in Cologne (DNW-KKK). It is a closed-circuit low-speed (M ≤ 0.38) wind tunnel (Figure 19-22). To realise high Reynolds numbers the wind

tunnel can be operated with nitrogen gas. The flow temperature can be set within in the range of 100 K ≤ T ≤ 300 K by injecting liquid nitrogen. Beneath the test section a model conditioning room is located from which the model support can be lifted up to the test section and enables access to the model without warming up the complete wind tunnel.

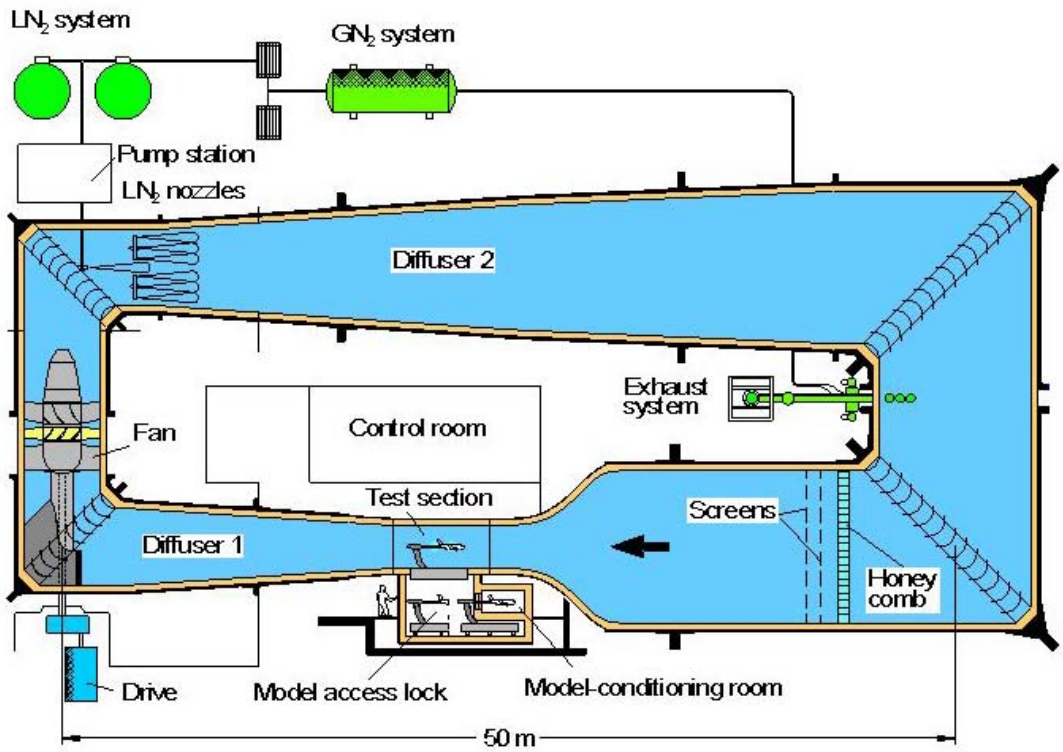

Figure 19-22: Sketch of Cryogenic Wind Tunnel in Cologne (DNW-KKK).

The delta-wing model of the TU-Munich was used for the tests, which is twice the size (c_r = 0.89 m) of NASA's ¾ scale 65° delta-wing model used in the DNW-TWG. The model is made of specific aluminium suitable for cryogenic temperatures and incorporates also interchangeable leading edge sections, so that the sharp as well as the medium radius ($r/\bar{c}$ = 0.0015) could be investigated. According to the geometry definitions a straight model sting was constructed by DLR which is connected to the 3d model support of the wind tunnel. The possible angle of attacks ranges from -15° to 30°. Similar to the model of NASA pressure taps are mainly arranged also at chord stations of 0.2, 0.4, 0.6, 0.8 and 0.95, whereas about 48 taps are equipped with pressure sensors to be able to measure instantaneous pressure fluctuations. However, these sensors are removed for the tests in the KKK resulting in a lower pressure tap resolution along the chord stations.

The model was applied with a Temperature Sensitive Paint (TSP) (Figure 19-23) which has a thickness of about 120 µm and is according to the scaling of the model twice the thickness of the PSP paint used for the measurements in the TWG. This coating was kept during the whole measurement campaign in the DNW-KKK.

Figure 19-23: The 65° Delta Wing of TU-Munich Coated with TSP in the Model Conditioning Room of the DNW-KKK.

19.4.1.2 Application of the Temperature Sensitive Paint and Infrared Techniques

While the Infrared technique [19-15] works very well at temperatures higher than 200 K (low Reynolds numbers) the TSP technique for cryogenic wind tunnels [19-4] can be applied at temperatures lower than 240 K (high Reynolds numbers). In both cases, these non-intrusive observation techniques detect boundary layer transitions on a model by measuring the temperature difference generated between laminar and turbulent boundary layers due to the difference of their convective heat transfer coefficients. This means that a small temperature difference between model and the flow in necessary. However, the naturally generated temperature difference is usually too small to create a large enough temperature differences on a model made of aluminium. Therefore, one needs to apply artificial enhancement of the laminar-to-turbulent temperature difference for cryogenic testing. This was achieved by warming up the delta wing model before every measurement series in the model-conditioning room beneath the test section. Then the model was quickly lifted up to the test section which was kept at the test temperature (205 K and 240 K) and the tunnel started blowing immediately. After the tunnel reached the test condition, the images were obtained using the temperature difference between the model and the flow before the model temperature could adapt to the flow temperature.

A single component TSP for cryogenic wind tunnels (cryoTSP) which was developed by JAXA [19-12] was applied to the model. The paint consists of a Ruthenium complex: Di(tripyridyl)ruthenium(II) (denoted here by Ru(trpy)) as a temperature sensitive luminophore and urethane polymer as a binder. Before applying the TSP the model was coated with a white screen layer for thermal insulation. After curing of the paint, the surfaces were polished carefully at each step to get sufficiently high smoothness (Ra < 0.1 µm).

For TSP two observation views were realised (Figure 19-24). The suction side of the complete model was captured by a camera (PCO-Pixelfly qe, 12 bit, 1392 x 1024 pixel) using a window in the top side of the test

section. A second setup (PCO-4000, 14 bit, 4008 x 2672 pixel) uses a side window to capture the leading edge. The model is illuminated using high power blue LED lamps (excitation wavelength: 425 nm < λ < 525 nm). Each camera was equipped with optical filters to select the TSP emission wavelength (580 nm < λ < 680 nm).

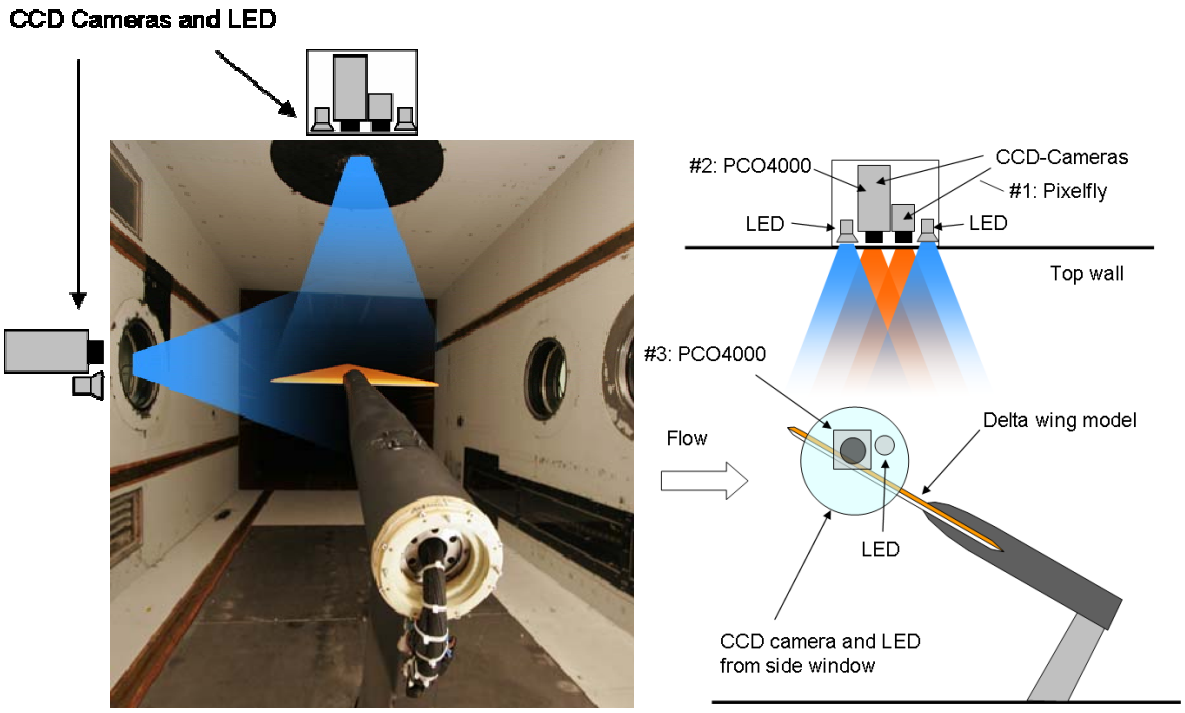

Figure 19-24: Delta Wing Model in the Test Section and Measurement Setups for TSP.

The Infrared measurements were performed separately. A single infrared camera (SC 3000 of FLIR Systems, 320 x 240 px, 50 fps, temperature resolution 20 mK) was placed behind the top window of the wind tunnel after removing the TSP arrangement. Also the glass window was changed by a special window made of Germanium which is transparent for infrared radiation in the wave length range of 10 µm. Since the spatial resolution of the infrared camera is much smaller that that of the TSP camera a infrared lens was chosen such that only about 40% of the model surface is captured within a single frame. Mainly the front part was recorded (Table 19-3), however, in some cases two camera adjustments were used to capture the front as well as the mid part of the model.

Table 19-3: Test Cases for IR Measurements in the DNW-KKK

Leading Edge	Sharp / Medium Radius
T	233 K / 258 K (sharp L.E.) 240 K (rounded L.E.)
M	0.113 / 0.147 (sharp L.E.) 0.051 / 0.077 / 0.103 / 0.154 (rounded L.E.)
R_{mac}	2 / 3 x 10^6 (sharp L.E.) 1/ 1.5 / 2 / 3 x 10^6 (rounded L.E.)
α (nominal)	α-sweeps from -5° to +28°

In the case of TSP an image post processing step is necessary to make the transition lines visible. A reference image taken at constant surface temperature distribution is divided by a run-image, which has the temperature difference between laminar and turbulent boundary layer superimposed and small temperature differences are amplified. For each test case (Table 19-4) a set of 12 run and reference images were taken from which an average is calculated for noise reduction. Also a dark image was subtracted from the averaged reference and run images to account for the camera dark current noise. Then, the ratio of the averaged reference and run images was taken. The obtained ratio images were further optimized to enhance the contrast in the images to make the flow phenomena on the delta model visible.

Table 19-4: Test Cases for TSP Measurements in the DNW-KKK

Leading Edge	Sharp / Medium Radius
T	205 K
M	0.042 / 0.063 / 0.083 / 0.125
R_{mac}	1 / 1.5 / 2 / 3 x 10^6
α (nominal)	5°, 10°, 13°, (18°, sharp L.E. only)

19.4.1.3 Application of Particle Image Velocimetry

To investigate the flow topology above the delta wing model with rounded leading edges at higher Reynolds numbers Stereo-PIV was also applied in the DNW-KKK under cryogenic conditions. A fixed measurement plane was used located at $x/c_r = 0.6$ and aligned perpendicular to the model axis for an angle of attack of 13°. The PIV laser (2 x 220 mJ) and the light sheet optics were attached to the side wall outside of the test section (Figure 19-25). One of the two available side windows is used to direct the light sheet to the model. The first PIV camera (PCO SensiCam QE, double-shutter, 1376 x 1060 px) is positioned within the test section using an thermal isolated and temperature controlled camera housing. The camera housing is mounted to the wind tunnel floor 4 m downstream the model such that the viewing angle to the light sheet is about 0°; i.e. 13° with respect to the wind tunnel axis. The second PIV camera is located outside the wind tunnel behind the second side wall window (s. Figure 19-25), which had a viewing angle of about 45° to the light sheet.

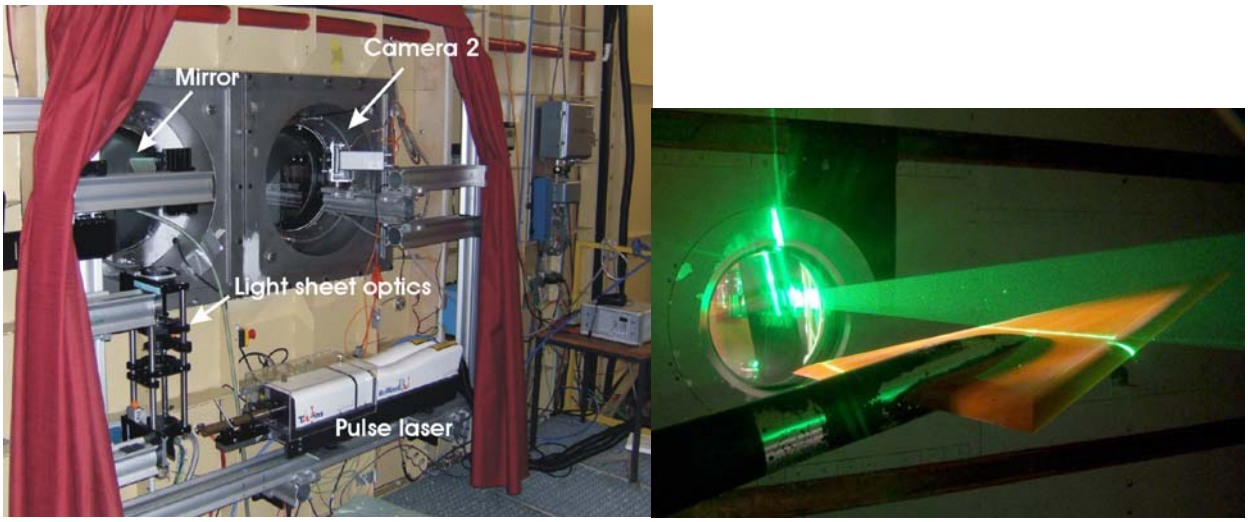

Figure 19-25: Left: Stereoscopic PIV Arrangement at the DNW-KKK. Camera 1 is located inside the wind tunnel 4 m downstream the model within a temperature controlled camera housing. Right: Light sheet above delta wing.

The test parameters were chosen according to the beforehand performed IR and TSP measurements (Table 19-5). Only the medium radius leading edge was investigated. Additional measurements were performed at very low temperatures of only 150 K to get data at higher Reynolds numbers of up to 6 million.

Table 19-5: Test Cases for PIV Measurements in the DNW-KKK

Leading Edge	Medium Radius
T	240 K / 205 K / 150 K
M	0.042 – 0175
R_{mac}	1 / 1.5 / 2 / 3 / 4 / 6 x 10^6
α (nominal)	5°, 10°, 13°, 16°, 18°, 20°, 23°, 25°, 28°

19.4.2 Preliminary Results from the DNW-KKK

The interpretation of the recorded TSP images as well as the IR images is not simple in the current case for two reasons. First, the model was not especially designed for transition detection measurements by means of comparing the different heat fluxes in a laminar and turbulent boundary layer. The model consists of different parts (exchangeable leading edge sections) and incorporates hollow spaces for instrumentation. This leads to non-uniform temperature distributions on the model surface which is reinforced by the fact that the model is made of aluminium of high heat conductivity and low thermal capacity. Second, also the strong vortices occurring above the delta wing produce a temperature signal at the surface, which is much higher than that of transition. Therefore, the measured temperature distributions are a superposition of the inhomogeneous cooling of the model, the temperature signal from the vortices and the laminar/turbulent transition. A separation of these signals is not always possible, so that the following analysis represents an incomplete description of the

transition lines above the delta wing. Future work on this topic will focus on the development of methods to separate the different signals.

In Figure 19-26 TSP results are shown of the delta wing with rounded leading edges for different Reynolds numbers and $\alpha = 5°$. The onset of the primary vortex has not taken place at this low angle of attack. The patterns in the TSP results in Figure 19-26 show two different effects leading to a transition from a laminar (bright areas) to a turbulent (dark areas) boundary layer. First, on the front part of the wing the transition line is located inboard of the leading edge; i.e. about 5 – 10% of the root chord length downstream the leading edge. The distance of the transition line from the leading edge slightly reduces downstream, which could be explained by an inboard movement of the free stream attachment line on the pressure side of the wing. Second, in the rear part of the wing a thin black line parallel to the leading edge can be observed. This indicates a closed flow separation caused by the high suction peaks at the rounded leading edge. Caused by this non-effective separation the boundary layer becomes turbulent; i.e. laminar separation and turbulent re-attachment. The TSP results show that the distance of the transition line to the leading edge reduces with increasing Reynolds number. Also the separation line in the rear part is shifted towards the leading edge. This can be also seen in Figure 19-27 showing results from the side view TSP camera.

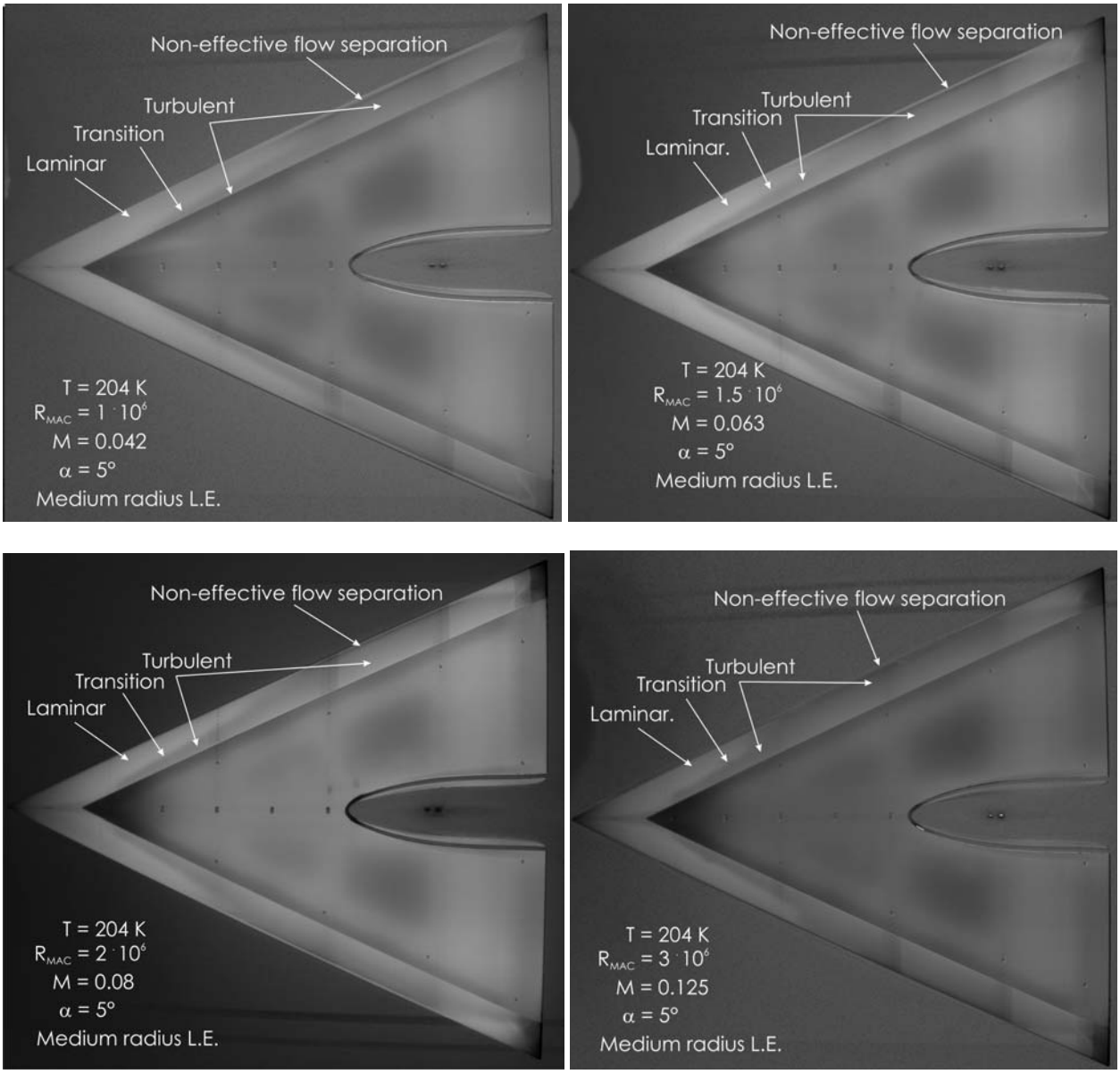

Figure 19-26: TSP Results of the Suction Side of the Delta Wing with Medium Radius Leading Edges at Low Angle of Attack of 5° for Different Reynolds Numbers.

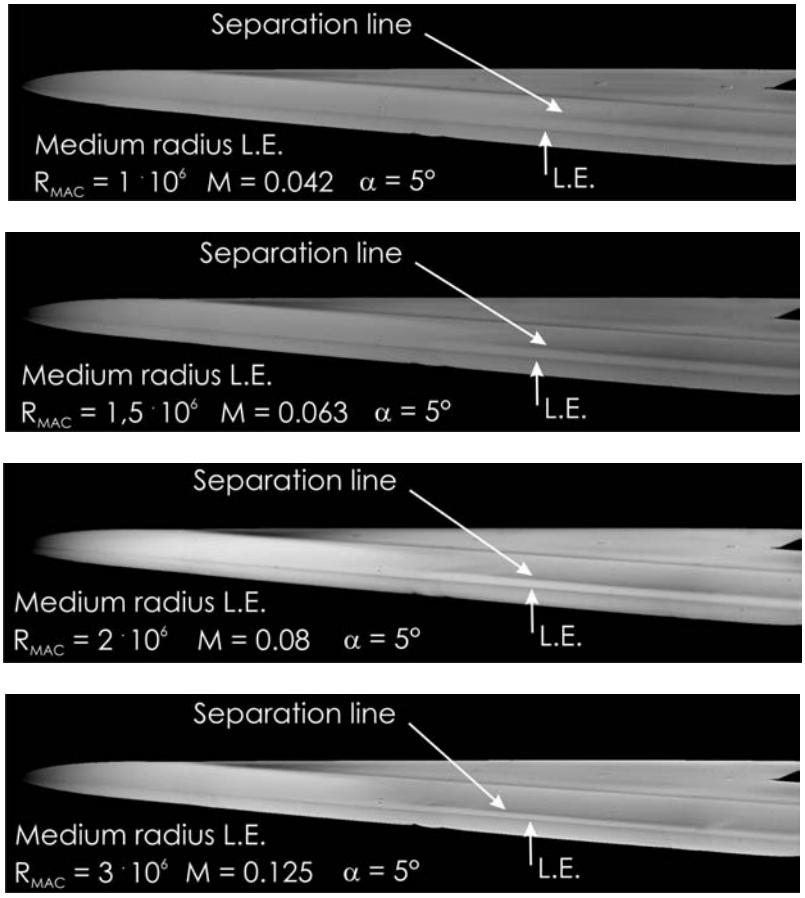

Figure 19-27: TSP Results from the Side View Camera Showing the Distribution along the L.E. of the Port Side of the Delta Wing at an Angle of Attack of 5° and Different Reynolds Numbers.

Because of the relatively low pixel resolution of the IR camera only a part of the wing was captured at one time. However, the camera's high sensitivity allowed for the recording of a complete alpha-sweep within a single run. Selected images of such an alpha sweep are shown in Figure 19-28 for a Reynolds number of $R_{mac} = 2$ million. The features as the development of the transition line on the front part of the delta wing, the non-effective flow separation at the leading edge and the occurrence of the primary vortex are indicated. At low angles of attack only the transition line can be seen which moves towards the leading edge and apex of the wing with increasing angle of attack. For $\alpha > 5°$ a thin black line gets visible in the temperature distribution close to the leading edge which is assumed to be a closed flow separation. The region of this non-effective flow separation moves towards the wing apex with increasing angle of attack accordingly to the increasing suction peaks at the leading edge.

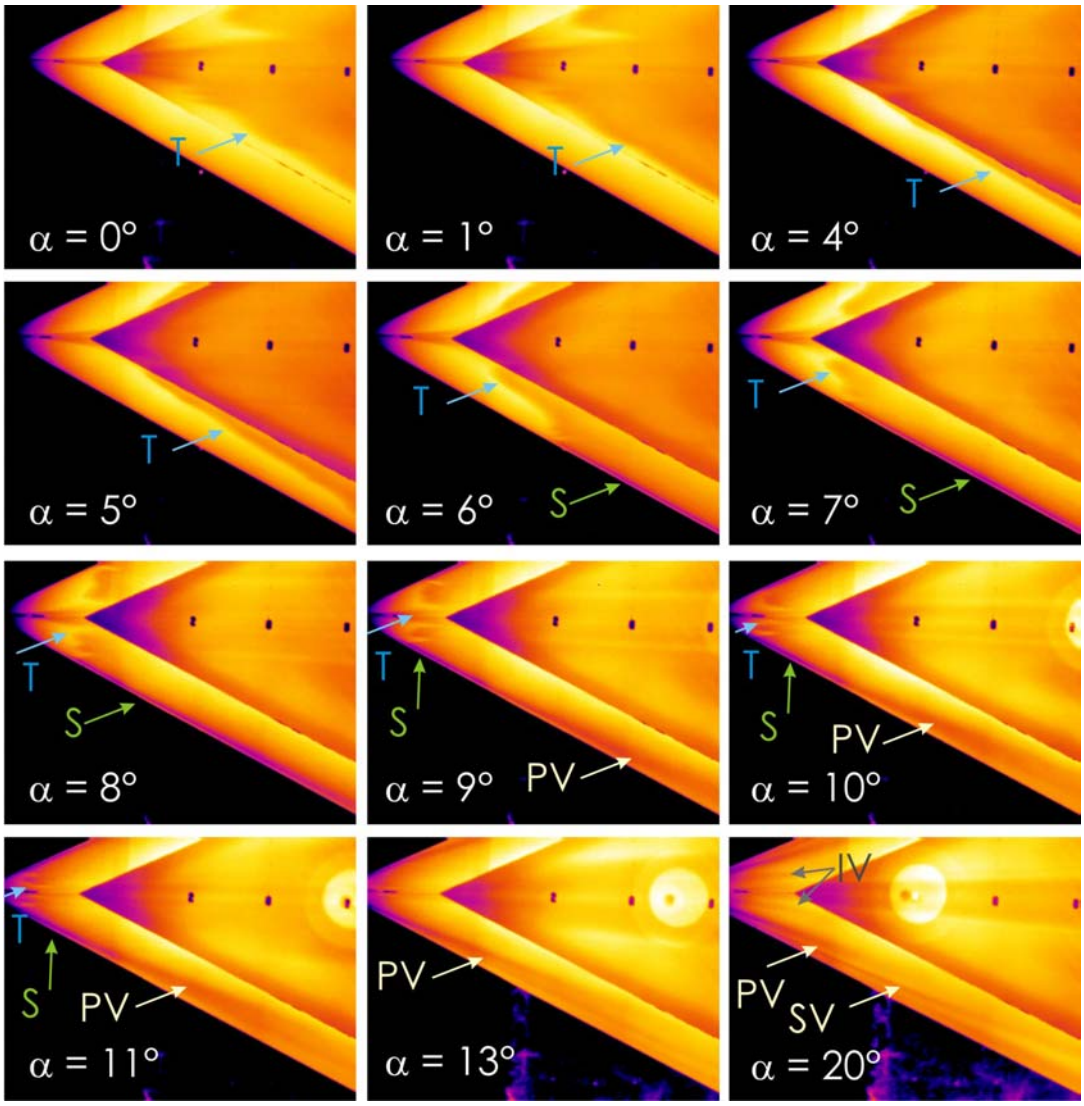

Figure 19-28: IR Results Showing the Temperature Distributions on the Suction Side of the Front Part of the Delta Wing with Rounded Leading Edges for R_{mac} = 2 Million, M = 0.103 (T = 240 K) for Different Angles of Attack. The three dot markers along the center line indicate the chord positions x/c_r = 0.2, 0.3 and 0.4 from left to right. (T) transition line (S) line of closed flow separation (PV) primary vortex (SV) secondary vortex (IV) inner vortex.

At an angle of attack of α = 9° the thin line in the temperature distribution broadens linearly downstream a point located at $x/c_r \cong 0.2$ which can be explained by the occurrence of the primary vortex. It seems that the primary vortex emerges from the closed flow separation; i.e. the non-effective flow separation changes into an effective flow separation forming the primary vortex. With the onset of the primary vortex a re-attachment line will occur inboard the vortex and beneath the vortex an outboard directed flow establishes. It was expected that a laminar boundary layer starts to develop at the re-attachment line and that a transition of the outboard directed flow occurs beneath the primary vortex probably after having passed the adverse pressure gradient [19-10]. Another transition line of the inboard directed flow should then be located somewhere inboard of the re-attachment line. However, no evidence for such a transition line can be seen within the TSP

and IR results. One reason for this could be the fact that the re-attachment line starts at the vortex origin which is located in the region where a closed flow separation occurs and transition takes place. Therefore, the boundary layer at the starting point of the re-attachment line can be assumed to be already turbulent or to be contaminated by turbulent structures. So, it is possible that a turbulent boundary layer develops along the complete re-attachment line of the primary vortex. Poll [19-23][19-24] investigated the transition on an inclined cylinder and observed transition on the attachment line when contaminated by turbulent structures.

Figure 19-29 shows the TSP results from the side view camera for α = 10° and 13° and R_{mac} = 2 million. The distribution at the leading edge for α = 13° has changed. First, downstream the origin of the primary vortex a dark area extends over the leading edge which indicates that the transition line is now located on the pressure side of the wing and the boundary layer is turbulent before the flow separates to form the primary vortex. Second, another structure can be observed at the apex upstream which is clearly separated from the signal of the primary vortex. This structure could be produced by another vortex, i.e. potentially by an inner vortex as observed in the results of the DNW-TWG measurements. A similar structure can be observed in the temperature distributions of the IR image at $\alpha = 20°$ close to the apex of the wing (Figure 19-28). However, the corresponding PIV results show no clear evidence for an existence of an inner vortex as described in Section 19.3.2. Only at a higher Reynolds number of R_{mac} = 6 million a weak inner vortex can be detected at α = 13° (Figure 19-30). Also the position of the primary vortex origin as detected by the PSP results for the TWG measurements (s. Figure 19-8, M = 0.4, R_{mac} = 2 million) differs from that as seen in the temperature distributions of the KKK measurements. The primary vortex starts more upstream in the case of the KKK; i.e. the primary vortex starts at $x/c_r \cong 0.15$ for R_{mac} = 2 million, M = 0.103 and α = 10° in the case of KKK (s. Figure 19-28) in comparison to an origin position of $x/c_r \cong 0.6$ for R_{mac} = 2 million, M = 0.4 and α = 10.1° in the case of TWG (s. Figure 19-7). This can be explained by the slightly different conditions in both wind tunnels, e.g. Mach number, or by small differences in the shape of the wind tunnel models. It was realized that the leading edge shape the TU-Munich deviates slightly from the given geometry resulting in a lower leading edge radius. This is in agreement with the observations mentioned above. The lower leading edge radius causes a more upstream located primary vortex and, therewith, a weaker inner vortical structure (s. Section 19.3.2).

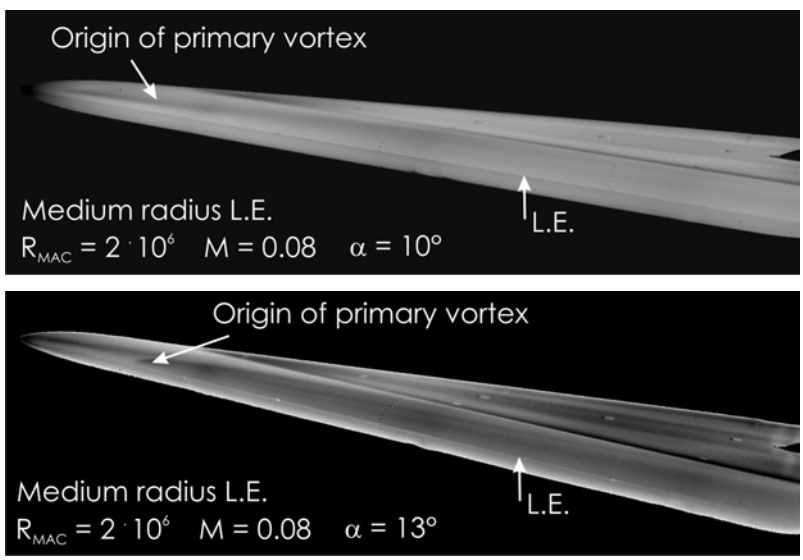

Figure 19-29: TSP Results from the Side View Camera Showing the Distribution along the L.E. of the Port Side of the Delta Wing at an Angle of Attack of 10° and 13°.

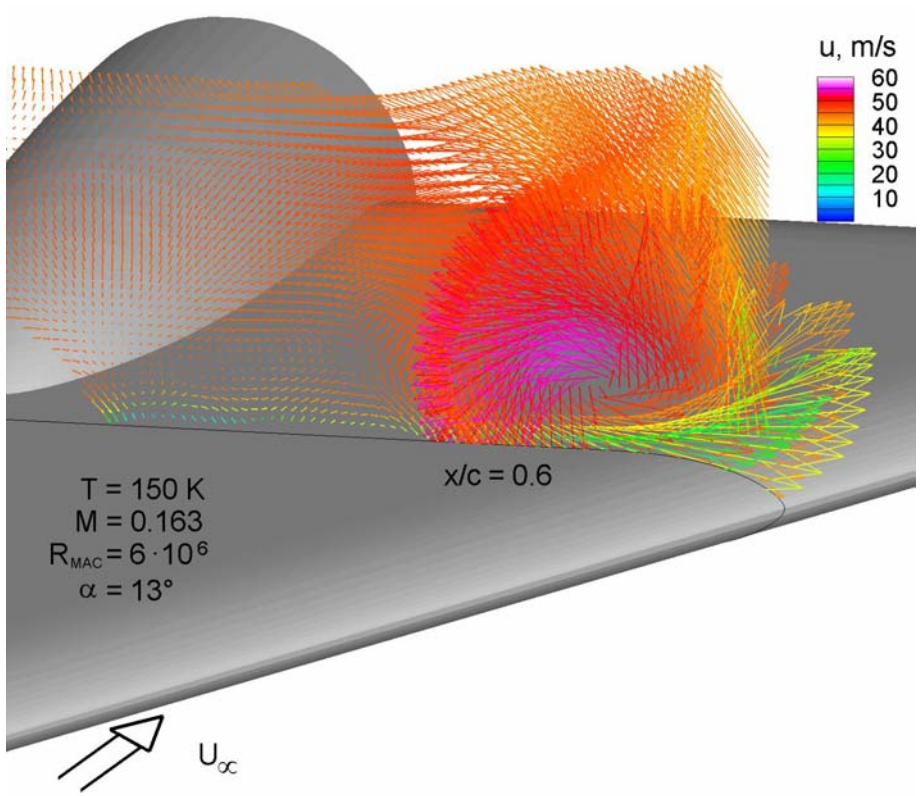

Figure 19-30: Time Averaged Velocity Field above the Delta Wing with Rounded Leading Edges for α = 13.3° and R_{mac} = 6 Million. The color of the vectors corresponds to the out-of-plane velocity.

19.5 CONCLUSIONS

Above the VFE-2 delta wing two different specific flow phenomena were observed in a transonic wind tunnel which could be investigated with the Pressure Sensitive Paint and Particle Image Velocimetry techniques. For the delta wing with rounded leading edges an inner vortical structure occurs above the delta wing at low angles of attack before a primary vortex develops; i.e. with an attached flow at the leading edge. This flat vortical structure develops close to the surface inboard of the leading edge and consists of several co-rotating vortices which increase in size downstream. The circulation strength of this structure increases with increasing angle of attack and seems to be in-sensitive to the Reynolds number as long as the onset of the outer primary vortex has not taken place. The flow at the rounded leading edge separates effectively at a specific angle of attack and a primary vortex is formed. The leading edge separation is promoted with reducing Reynolds number or increasing Mach number. Therewith, the origin of the primary vortex origin moves upstream. The occurrence of the primary vortex leads to a detachment of the outboard located vortices of the inner vortical structure. A new circular inner vortex is formed downstream the origin of the primary vortex. Both co-rotating vortices remain separated downstream. However, vorticity is fed only into the outer primary vortex so that the inner vortex keeps its size and decreases slightly in circulation strength downstream by viscous effects. At the beginning the flow re-attaches and again separates form the surface between both vortices. Further downstream a stagnation point can be observed in the cross flow fields such that an outboard directed flow exists at the surface underneath and between both vortices. Since vorticity is fed into the inner vortical structure only upstream the primary vortex the circulation strength of the inner vortex decreases with an upstream movement of the primary vortex; i.e. with

increasing angle of attack and decreasing Reynolds number. This probably is the reason why the inner vortex could not be observed for the delta wing with sharp leading edges where the flow separation is fixed at the leading edge and the primary vortex starts always close to the wing apex.

In the transonic case the flow field above the delta wing reaches supersonic speeds which lead to the formation of cross-flow and terminating shock waves. The results show at high angles of attack a sudden change of the surface pressure distributions within a range of increase of the angle of attack of only 0.2°. The velocity distributions show that a vortex breakdown occurs above the delta wing at about 65% of the root chord. This could be explained by an interaction between shock waves and the primary vortex. One terminating shock wave could be detected using the pressure distributions in front of the sting fairing; i.e. at about 55% of the root chord.

The activities within VFE-2 show also useful interactions between computational and experimental disciplines. After the first measurement campaign the PSP distributions clearly show the footprints of two separate suction peaks. However, the PSP results do not answer the question which flow produces the inner peak. On basis of the PSP result parameters for flow computation could be optimized (Fritz, EADS Munich) and the inner vortex came out. In turn the CFD result could be used for setting up parameters of the flow field investigation by means of PIV which verifies the CFD result. However, the CFD computations show a strong sensitivity against the location of transition. This leads to the performance of IR and TSP measurements for which first results are available.

19.6 ACKNOWLEDGEMENTS

The International Vortex Flow Experiment 2 (VFE-2) is indebted to NASA and the Technical University of Munich for their readiness to provide the wind tunnel models within the scientific program of the Task Group AVT-113. The authors would like to thank Dr. J. Luckring (NASA, Langley) for his support of the model loan agreement and transfer of the model form NASA Langley to DLR Göttingen. The authors would also like to thank Mr. Furman (TU Munich) for helping preparing the model in the DNW-KKK. The authors were also much obliged to the wind tunnel test teams of DNW-TWG and DNW-KKK for assistance. Special thanks go to Prof. Dr. D. Hummel (TU Braunschweig). He initiated the Vortex Flow Experiment 2 and took part in the VFE-2 wind tunnel test campaigns at Göttingen and Cologne. The authors also would like to thank U. Henne, W. Sachs, and A. Wiedemann for performing the PSP measurements and J. Agocs, A. Heider, H. Mattner, T. Kirmse and D. Otter for performing the PIV measurements and Y. Egami and U. Fey for performing the TSP measurements.

19.7 REFERENCES

[19-1] Carmer, C.F. von, Konrath, R., Schröder, A. and Monnier, J.-C.: *Identification of Vortex Pairs in Aircraft Wakes from Sectional Velocity Data*, Exp. Fluids 44: 367-380, 2008.

[19-2] Chu, J. and Luckring, J.M.: *Experimental Surface Pressure Data Obtained on 65° Delta Wing Across Reynolds Number and Mach Number Ranges*, NASA TM 4645, 1996.

[19-3] Drougge, G.: *The International Vortex Flow Experiment for Computer Code Validation*, ICAS-Proceedings 1988, Vol. 1, pp. XXXV-XLI, 1988.

[19-4] Egami, Y., Fey, U., Klein, Chr., Sitzmann, M. and Wild, J.: *Transition Detection on High-Lift Devices in DNW-KKK by Means of Temperature Sensitive Paint*, Proc. of 12th International Symp. on "Flow Visualization", [CD-ROM], Göttingen, 2006.

[19-5] Elsenaar, A., Hjelmberg, L., Bütefisch, K.-A. and Bannink, W.J.: *The International Vortex Flow Experiment*, AGARD-CP-437, Vol.1, pp. 9-1 to 9-23, 1988.

[19-6] Elsenaar, A. and Bütefisch, K.-A.: *Experimental Study on Vortex and Shock Wave Development on a 65° Delta Wing*, Proc. IUTAM Symposium Transonicum III, Göttingen, 1988.

[19-7] Görtz, S. and Rizzi, A.: *Computing the High-Alpha Aerodynamics of Delta Wings – Evaluation and Analysis*, AIAA Paper 01-0115, 2001.

[19-8] Hilgenstock, A. and Vollmers, H.: *On the Simulation of Compressible Turbulent Flows Past Delta Wing, Delta Wing-Body and Delta Wing-Canard*, AGARD-CP-494, pp. 7-1 to 7-13, 1991.

[19-9] Hummel, D. and Redeker, G.: *A New Vortex Flow Experiment for Computer Code Validation*, RTO AVT Symposium on "Vortex Flow and High Angle of Attack Aerodynamics", Loen, Norway, 7-11 May 2001, Meeting Proceedings RTO-MP-069 (I), SYA 8-1 to 8-31, 2003.

[19-10] Hummel, D.: *Effects of Boundary Layer Formation on the Vortical Flow Above Slender Delta Wings*, RTO Specialists' Meeting on "Enhancement of NATO Military Flight Vehicle Performance by Management of Interacting Boundary Layer Transition and Separation", Prague, Czech Republic, 4-7 October 2004, Meeting Proceedings RTO-MP-AVT-111, pp. 30-1 to 30-22, 2004.

[19-11] Hummel, D.: *The Second International Vortex Flow Experiment (VFE-2) – Objectives and First Results*, Proceedings of the 2nd International Symposium on "Integrating CFD and Experiments in Aerodynamics", Cranfield University (Shrivenham), UK, 5-6 September, pp. 1-12, 2005.

[19-12] Iijima, Y., Egami, Y., Nishizawa, A., Asai, K., Fey, U. and Engler, R.H.: *Optimization of Temperature-Sensitive Paint Formulation for Large-Scale Cryogenic Wind Tunnels*, Proc. of 20th International Congress on "Instrumentation in Aerospace Simulation Facilities (ICIASF)", Göttingen, Germany, pp. 70-76, 2003.

[19-13] Klein, C., Engler, R.H., Henne, U. and Sachs, W.: *Application of Pressure-Sensitive Paint for Determination of the Pressure Field and Calculation of the Forces and Moments of Models in a Wind Tunnel*, Exp. Fluids 39: 475-483, 2005.

[19-14] Klein, C., Sachs, W., Henne, U., Engler, R.H., Wiedemann, A. and Konrath, R.: *Development of PSP Technique for Application on the VFE-2 65° Delta Wing Configuration in Sub- and Transonic Flow*, AIAA-Paper 2006-0059, 2006.

[19-15] Kompenhans, J., Agocs, J., Egami, Y., Engler, R., Fey, U., Frahnert, H., de Groot, K., Henne, U., Kirmse, T., Klein, Ch., Klinge, F., Konrath, R., Mattner, H., Otter, D., Pallek, D., Sachs, W., Schröder, A. and Stasicki, B.: *Recent Developments of Image Based Measurement Methods for Application to Transonic Flows in Industrial Wind Tunnels*, ZHU, Zi-qiang [Ed.]: Chinese Journal of Aeronautics, EWHSFF2005, Vol. 19 (No. 2), AAAS, S. 115-125, ISBN CN 11-1732/V, ISSN 1000-9361, 2006.

[19-16] Konrath, R., Klein, C., Engler, R.H. and Otter, D.: *Analysis of PSP Results Obtained for the VFE-2 65° Delta Wing Configuration at Sub- and Transonic Speed*, AIAA-Paper 2006-0060, 2006.

[19-17] Konrath, R., Schröder, A. and Kompenhans, J.: *Analysis of PIV Results Obtained for the VFE-2 65° Delta Wing Configuration at Sub- and Transonic Speeds*, AIAA-Paper 2006-3003, 2006.

[19-18] Konrath, R., Klein, C., Schröder, A. and Kompenhans, J.: *Combined Application of Pressure Sensitive Paint and Particle Image Velocimetry to the Flow Above a Delta Wing*, Exp. Fluids 44: 357-366, 2008.

[19-19] Konrath, R., Klein, C. and Schröder, A.: *PSP and PIV Investigations on the VFE-2 Configuration in Sub- and Transonic Flow*, AIAA-Paper 2008-379, 2008.

[19-20] Luckring, J.M.: *Reynolds Number, Compressibility, and Leading-Edge Bluntness Effects on Delta-Wing Aerodynamics*, ICAS Proceedings, Paper 4.1.4, 2004.

[19-21] Luckring, J.M.: *Compressibility and Leading-Edge Bluntness Effects for a 65° Delta-Wing*, AIAA Paper 2004-0765, 2004.

[19-22] Morton, S.A., Forsythe, J.R., Mitchell, A.M. and Hajek, D.: *Detached-Eddy Simulations and Reynolds-Averaged Navier-Stokes Simulations of Delta Wing Vortical Flowfields*, AIAA Paper 2002-0587, 2002, and J. Fluids Eng. Vol. 124, No. 4, pp. 924-932, 2002.

[19-23] Poll, D.I.A.: *Some Observations of the Transition Process on the Windward Face of a Long Yawed Cylinder*, J Fluid Mech., Vol. 150, pp. 329-356. 1985.

[19-24] Poll, D.I.A.: *Transition in the Infinite Swept Attachment Line Boundary Layer*, The Aeronautical Quarterly, Vol. 30, Cranfield, pp. 607-629. 1979.

[19-25] Schiavetta, L., Boelens, O.J. and Fritz, W.: *Analysis of Transonic Flow on a Slender Delta Wing Using CFD*, AIAA-Paper 2006-3171, 2006.

[19-26] Schröder, A., Agocs, J., Frahnert, H., Otter, D., Mattner, H., Kompenhans, J. and Konrath, R.: *Application of Stereo PIV to the VFE-2 65° Delta Wing Configuration at Sub- and Transonic Speeds*, AIAA-Paper 2006-3486, 2006.

[19-27] Wedemeyer, E.: *Vortex Breakdown*, Proc. AGARD-LS-121, High Angle of Attack Aerodynamics, pp. 9-1 to 9-17, 1982.